Molecular profiles, sources and lineage restrictions of stem cells in an annelid regeneration model

Alexander W. Stockinger[1,2,3,4,5,*], Leonie Adelmann[1,2,3,4,5,*], Martin Fahrenberger[1,3,4,6,7], Christine Ruta[8], B. Duygu Özpolat[9,#], Nadja Milivojev[1,2,3,4,5], Guillaume Balavoine[9,,@], Florian Raible[1,2,3,@]

1, Max Perutz Labs, Vienna Biocenter Campus (VBC), Vienna, Austria
2, University of Vienna, Center for Molecular Biology, Department of Genetics and Microbiology, Vienna, Austria
3, Research Platform Single-Cell Regulation of Stem Cells (SinCeReSt), University of Vienna, Vienna, Austria
4, Vienna Biocenter PhD Program, a Doctoral School of the University of Vienna and the Medical University of Vienna, Vienna, Austria
5, PhD Programme Stem Cells, Tissues, Organoids – Dissecting Regulators of Potency and Pattern Formation (SCORPION), University of Vienna, Vienna, Austria
6, Center for Integrative Bioinformatics Vienna (CIBIV), University of Vienna and Medical University of Vienna, Austria
7, Medical University of Vienna, Max Perutz Labs, Vienna, Austria.
8, Institute of Biology, Federal University of Rio de Janeiro, Rio de Janeiro, Brazil
9, Université de Paris Cité, CNRS, Institut Jacques Monod, Paris, France

* these authors contributed equally to this work
# present address: Department of Biology, Washington University in Saint Louis, MO, USA

@ correspondence for transgenic work: guillaume.balavoine@ijm.fr
@ correspondence for single-cell analyses: florian.raible@univie.ac.at

Abstract

Regeneration of missing body parts can be observed in diverse animal phyla, but it remains unclear to which extent these capacities rely on shared or divergent principles. Research into this question requires detailed knowledge about the involved molecular and cellular principles in suitable reference models. By combining single-cell RNA sequencing and mosaic transgenesis in the marine annelid *Platynereis dumerilii*, we map cellular profiles and lineage restrictions during posterior regeneration. Our data reveal cell-type specific injury responses, re-expression of positional identity factors, and the re-emergence of stem cell signatures in multiple cell populations. Epidermis and mesodermal coelomic tissue produce distinct putative posterior stem cells (PSCs) in the emerging blastema. A novel mosaic transgenesis strategy reveals both developmental compartments and lineage restrictions during regenerative growth. Our work supports the notion that posterior regeneration involves dedifferentiation, and reveals molecular and mechanistic parallels between annelid and vertebrate regeneration.

Introduction

The ability of some animals to regenerate missing body parts is a fascinating phenomenon. Whereas the regenerative ability of mammals is generally limited to individual cell types or a few specific organs, other animals are capable of rebuilding their entire body from mere fragments of tissue. Complex tissue regeneration can be observed in almost all clades of bilaterian life and might therefore reflect an ancient capacity [1,2]. This regenerative process usually involves the formation of an epimorphic, proliferative cell mass called blastema [3]. The cellular sources and molecular properties of blastema cells, however, differ between available model systems. For example, whereas some invertebrates like the planarian *Schmidtea mediterranea* form their blastemas from totipotent stem cells [4], other regenerative models employ less potent stem cells, such as uni- or oligopotent progenitors, and make use of dedifferentiation, transdifferentiation or a combination of these processes [3,5–7]. While molecular similarities between these regenerative strategies can be observed across phyla, we still lack comprehensive data on representative species to uncover whether or not these similarities indicate true homologies [3]. Defining molecular signatures of blastema formation in accessible model systems and regeneration paradigms will be a key requirement for such comparisons.

Annelids show particular promise as models to inform mechanisms and pathways of blastema-based regeneration. Many species within this clade exhibit the ability to regenerate large parts of their primary body axis. Annelids are phyletically well-positioned for long-range comparisons with other lophotrochozoan clades, such as planarians, as well as deuterostomes (which include vertebrates). Likewise, comparisons between different annelids provides an avenue to assess modulation of regenerative capacities within the clade [8–12]. This makes annelids ideal models to assess both commonalities and differences in regenerative processes.

The nereidid worm *Platynereis dumerilii* has a long history as a model system for regeneration and regenerative growth [8,9]. This bristleworm can be continuously bred in the laboratory, and offers a variety of molecular and genetic tools for analysis, including transcriptomic profiling, multiplexed detection of RNAs in fixed specimens, and transgenic manipulation [9,13–17].

During normal development, *Platynereis* grows by continuous segment addition, which involves a dedicated ring-shaped “segment addition zone” (SAZ) located between the posterior-most segment and the post-segmental pygidium [18]. Molecularly, the SAZ harbors putative posterior stem cells (PSCs) that express members of the germline multipotency program (GMP) [19], such as *piwi*, *vasa* and *nanos*.

Upon amputation across the primary body axis, *Platynereis* re-establishes a functional SAZ which then produces the missing posterior segments. Morphologically, this process has been well characterized (reviewed in [8,10,20]): in a first, rapid response to injury, the gut seals the wound. In a second step, epidermal cells cover the injury under a wound epithelium, followed by the formation of a largely undifferentiated blastemal cell mass, from which the new SAZ emerges. After this point, new segments are added and the animals grow faster than during regular development [10,21].

The source of stem cells during regeneration has been of long-standing interest. Tissue-residual stem cells, as well as the de- and trans-differentiation of somatic cells have been observed as sources of animal blastemas (reviewed in [5,6,22]). While adult stem cells as a source have been described in some invertebrates, such as planarians (see above), most data within annelids point towards de-differentiation as a likely source of stem cells during regeneration (reviewed in [8,20]), with few exceptions found among the class *Clitellata* (reviewed in[10]).

In *Platynereis*, early cytological evidence already suggested the amputation-induced emergence of new stem cells in differentiated tissues such as the wound-adjacent epidermis. This process has classically been referred to as "re-embryonalisation" [23]. Re-amputation, along different planes of posterior regenerates that had been labeled using EdU (5'-ethynyl-2'-deoxyuridine) incorporation, suggests that resident proliferating cells do not contribute disproportionately to the regenerating SAZ. It has therefore been suggested that the *Platynereis* SAZ regenerates from wound-adjacent, presumably differentiated cells, which activate GMP gene expression and re-enter the cell cycle after injury [21].

24 hours post amputation (hpa), the wound is covered with an epithelium. This stage can be reached even when proliferation is inhibited [21]. At 24 hpa, several genes usually found in the SAZ of uninjured animals, such as the ectodermal PSC marker *hox3* and the GMP members *piwi* and *myc*, are expressed *de novo* in and near the wound.

After 48 hpa, injured worms have formed a blastema, at which point proliferation increases markedly [21]. Bulk transcriptomic profiling and an analysis of epigenetic factor expression during regeneration support the idea that these steps are accompanied by chromatin remodeling [24,25]. While other cell sources, such as quiescent and currently undiscovered residual stem cells can not be fully excluded, these findings support the notion of differentiated cells providing the source for a regenerating SAZ through dedifferentiation.

Currently available data lack the cellular resolution to identify tissue- and cell type specific properties of regeneration in *Platynereis*, including the transcriptional profile of cells responding to injury with chromatin remodeling and GMP gene expression as outlined above.

Additionally, no information regarding the differentiation potential / lineage restriction of *Platynereis* PSCs is currently available, further complicating comparative analyses. To gain deeper and unbiased insight into this process and enable cross-species comparisons of blastema based regeneration, molecular profiling at cellular resolution and clonal information of lineage restriction are required.

Here, we follow a dual approach of single-cell RNA sequencing and transgenesis experiments throughout posterior regeneration to address these challenges. By sampling single-cell transcriptomes at multiple regenerative stages and comparing them to wound-adjacent tissue right after injury, we are able to derive a comprehensive, time-resolved map of cellular profiles over the regenerative process. We detect cell-type specific injury responses and re-expression of positional identity factors. We also uncover that multiple wound-adjacent cell populations start expressing stem cell related genes and enter the cell cycle upon injury, consistent with the notion that these cells undergo dedifferentiation.

Investigating signature genes for two of these populations, we identify the epidermis and mesodermal coelomic tissue as two likely source tissues that produce distinct PSCs in the segment addition zone. Capitalizing on a novel mosaic transgenesis strategy, we are able to identify both developmental compartments and restrictions in cell lineages throughout posterior growth and regeneration. We demonstrate that the SAZ of *Platynereis dumerilii* harbors separate pools of lineage-restricted PSCs and that these pools are regenerated from cells originating from distinct embryonic germ layers. Our combined datasets provide a detailed view of the sources, molecular signatures and differentiation potential of major cell types in the blastema, and reveal molecular and mechanistic similarities between annelid and vertebrate regeneration.

Results

A temporally resolved single cell atlas reveals the dynamic transcriptional landscape of posterior regeneration

To establish a first unbiased, in-depth analysis of the transcriptomic landscape of individual cell populations during posterior regeneration in annelids, we devised a suitable sampling scheme. For this, we induced posterior regeneration by removing approximately ⅓ of the animals' posterior tissue, including the SAZ and its rapidly proliferating progeny, amputating between segments 30 and 31. For sampling, we then isolated the posteriormost segment along with any newly regenerated tissue at distinct time points after amputation (Supplementary Fig. 1a).

157 We reasoned that inclusion of the last non-amputated segment in these analyses would not
158 only provide us with data on differentiated cell types, but also allow us to detect any
159 molecular signatures associated with the response of this segment to the adjacent wound.
160 To assess whether this sampling scheme captured relevant molecular events in the early
161 phases of blastema formation, we first performed a bulk RNA sequencing experiment, in
162 which the total mRNA of each sampling time point was sequenced from biological triplicates.
163 By using an unbiased gene-clustering approach, we determined seven major categories of
164 gene expression dynamics over the first three days of regeneration, including four categories
165 in which gene expression increased after amputation, with differences in the point of onset
166 and kinetics (Supplementary Fig. 1b). Genes in these categories include known markers for
167 stem cells and the SAZ, as well as proliferation-related transcripts (Supplementary Fig. 1b).
168 These findings are consistent with previous observations [21,24,25] and confirmed that our
169 sampling strategy could be used to capture relevant molecular processes.
170
171 Based on these results, we devised a similar sampling scheme to build a comprehensive
172 single cell atlas of posterior regeneration (Fig. 1a). We obtained single cells from multiple
173 dissociated samples, representing five distinct stages of regeneration. These spanned from
174 freshly amputated individuals (0 hpa, equivalent to uninjured trunk segments, but not the
175 posterior-most tissues such as the SAZ and its immediate progeny) to 72 hpa, corresponding
176 to the onset of rapid proliferation in the regenerated SAZ [21], increasing the temporal
177 resolution in early regenerative stages by adding a 12 hpa timepoint (Fig. 1a). After removing
178 outlier and low-quality cells, we obtained a total of 80,298 transcriptomes of individual cells,
179 sampled in two independent biological replicates of 4 and 5 timepoints, respectively
180 (Supplementary Data 1). Even though the sampling timepoints of this single cell experiment
181 slightly differed from those sampled in bulk (see above), we compared the two datasets
182 using a correlation analysis. Despite the use of different sampling, sequencing and
183 processing techniques, all replicates correspond most strongly with those in the respective
184 other dataset sampled at the closest time point (Supplementary Fig. 1c).

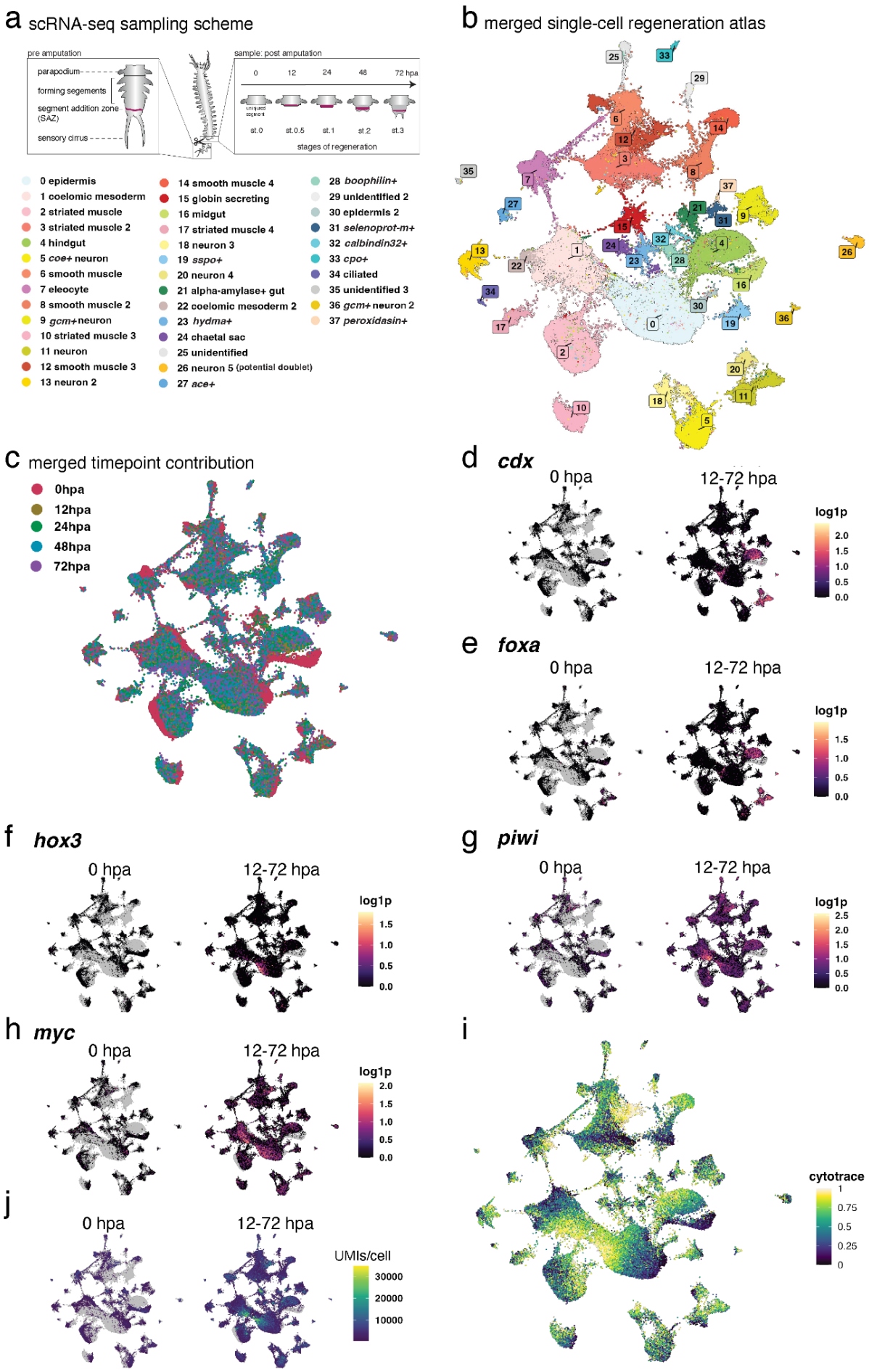
a scRNA-seq sampling scheme
pre amputation
parapodium
forming segements
segment addition zone (SAZ)
sensory cirrus
sample: post amputation
0
12
24
48
72 hpa
st.0
st.0.5
st.1
st.2
st.3
stages of regeneration
0 epidermis
1 coelomic mesoderm
2 striated muscle
3 striated muscle 2
4 hindgut
5 coe+ neuron
6 smooth muscle
7 eleocyte
8 smooth muscle 2
9 gcm+neuron
10 striated muscle 3
11 neuron
12 smooth muscle 3
13 neuron 2
14 smooth muscle 4
15 globin secreting
16 midgut
17 striated muscle 4
18 neuron 3
19 sspo+
20 neuron 4
21 alpha-amylase+ gut
22 coelomic mesoderm 2
23 hydma+
24 chaetal sac
25 unidentified
26 neuron 5 (potential doublet)
27 ace+
28 boophilin+
29 unidentified 2
30 epidermis 2
31 selenoprot-m+
32 calbindin32+
33 cpo+
34 ciliated
35 unidentified 3
36 gcm+ neuron 2
37 peroxidasin+
b merged single-cell regeneration atlas
c merged timepoint contribution
0hpa
12hpa
24hpa
48hpa
72hpa
d cdx
0 hpa
12-72 hpa
log1p
e foxa
0 hpa
12-72 hpa
log1p
f hox3
0 hpa
12-72 hpa
log1p
g piwi
0 hpa
12-72 hpa
log1p
h myc
0 hpa
12-72 hpa
log1p
i
cytotrace
j
0 hpa
12-72 hpa
UMIs/cell

185

Figure 1. A temporally resolved single cell atlas reveals the dynamic transcriptional landscape of cell populations during posterior regeneration. (a) Sampling scheme illustrating posterior amputation and sampling timepoints, ranging from 0 hours post amputation (0 hpa, equivalent to a regular trunk segment) to 72 hpa, matching morphologically defined stages (st. 0 to 3). **(b)** UMAP visualization of cells, annotated by tentative cell type / population identity. **(c)** UMAP visualization showing the regenerative timepoint at which cells were sampled. **(d,e)** UMAP visualizations showing the expression of posterior identity markers (*cdx, foxa*) on the merged dataset, contrasting the freshly amputated sample (left) with the post-amputation time points (right) **(f-i)** similar UMAP visualizations, highlighting the changes in expression of stem-cell related genes (*hox3*, *piwi*, *myc*) (f-h) as well as the emergence of hypertranscriptomic cells (UMIs/cell) (i).(j) UMAP visualization of CytoTRACE values (calculated per cluster; high level indicates high differentiation potential).

Single-cell data comprising multiple replicates or biological samples might suffer from batch effects, where technical differences between sampling rounds could overshadow biologically meaningful differences between samples or cell types [26]. To counter this effect and minimize technical variations, we took advantage of the recent establishment of a combined cell fixation and storage protocol (ACetic-MEthanol/ACME) that is compatible with single-cell sequencing [27]. The adaptation of this protocol for our *Platynereis* regenerate paradigm allowed us to sort, process and sequence cells from all sampled stages in parallel. We subsequently used standard single-cell RNA sequencing (scRNA-seq) analysis methods to process the joined data-set (see Methods).

Unbiased clustering of the cells resulted in 38 transcriptionally distinct clusters. The comparison between biological replicates and timepoints did not suggest any batch effect affecting cluster formation (Supplementary Data 1, Supplementary Fig. 2a-e). The resulting clusters, as illustrated on a uniform manifold approximation and projection (UMAP) visualization [28] (Fig. 1b), correspond to cell populations of similar transcriptomic profiles. Algorithmic prediction [29] identifies one cluster (cluster 26) as the possible product of doublet formation, so this cluster was not investigated further (Supplementary Data 1). We annotated these populations based on the identities of cluster-specific marker genes, and their expression levels of known annelid cell-type markers. In total, we annotated 35 of the clusters, either as known cell populations, or based on their most diagnostic marker gene (Fig. 1b, see details in Supplementary Data 2 and 3).

As each sampled tissue contains the segment adjacent to the injury site, we were able to identify a variety of cell types in our dataset. For example, an investigation of genes previously used for assigning different *Platynereis* muscle cell types [30], allowed us to distinguish several populations of smooth (clusters 3, 6, 8, 12 and 14) and striated (clusters 2, 10, and 17) muscle. Even less abundant cell types, such as chaetal sac cells (cluster 24) which form the bristle worm's chitinous bristles [31,32] and extracellular globin-secreting cells (cluster 15) [33], were identified as distinct populations. This shows that our approach yielded a high-quality cell atlas containing biologically meaningful clusters of cell populations and with sufficient sensitivity to resolve rare and poorly understood cell types.

Molecular repatterning and emerging stem cell-like properties in distinct cell populations

As outlined above, deconvolving the dynamic injury response to individual cell populations in an annelid is expected to advance our understanding of regeneration in an evolutionary context. By capitalizing on the temporal information embedded in each transcriptome of our dataset (Fig. 1c), we were able to perform comparisons of gene expression within cell populations across time.

A common challenge in complex tissue regeneration is the re-establishment of appropriate positional information, such as the position along the antero-posterior axis. To test whether our dataset could be used to identify the individual cell types involved in repatterning, we analyzed the expression of several transcription factors involved in posterior identity. Bulk RNA sequencing of posterior regeneration and unbiased clustering of genes with similar expression dynamics using mfuzz (Supplementary Fig. 1b) revealed the presence of genes encoding posteriorly expressed transcription factors such as *caudal* (*cdx*), *distalless* (*dlx*) and *foxA*, in gene sets upregulated after injury. This is consistent with previous suggestions that early steps in annelid regeneration include a morphallactic adjustment of positional values [34].

Using the single cell atlas, we were able to add cellular resolution to this process. For example, cells of midgut identity (cluster 16) are only found in the freshly amputated sample (0 hours post amputation, hpa), subsequently yielding to a population (cluster 4) demarcated by *foxA* and *cdx* as hindgut after injury (Fig. 1d,e). This morphallactic process of gut posteriorization indicated by *foxA* has previously been proposed in *Platynereis* [35], demonstrating the validity of our *in silico* approach. In addition, a subset of neuronal populations (clusters 11, 20) expresses *cdx* and *foxA* shortly after injury (Fig. 1d, e), while two other populations (clusters 0, epithelium; cluster 9, *gcm+* neurons) started to express *dlx* (Supplementary Fig. 3a). Similarly, we observed a molecular shift in presumptive smooth muscle cells from cluster 14 (pre-injury) to clusters 8 (post-injury), involving genes like *thrombospondin*, *rho kinase* [36] and *octopamine receptor 2*, which play a role in muscle attachment, function and regeneration in other species [37–40] (Supplementary Data 3).

As these data supported our approach to reconstructing temporal dynamics, we next investigated the expression of stem cell related genes after posterior injury. We reasoned that if stem cells are, at least in part, regenerated by dedifferentiation or activation of wound-adjacent cells, we should detect cell populations that are already present at 0 hpa, but start to express stem cell and proliferation-related markers only after injury.

265 To assess this point, we first investigated the expression of the homeobox gene *hox3*, whose
266 transcripts are rapidly upregulated in posterior regeneration of *Platynereis dumerilii* [41] and
267 mostly restricted to a population of PSCs that are generally referred to as ectodermal PSCs
268 in accordance with their presumed developmental origin [18,21]. Whereas homeostatic trunk
269 cells (0 hpa) are almost entirely devoid of *hox3* expression, we could detect a strong and
270 mostly cluster-specific upregulation of this gene in post-injury time points of cluster 0 (Fig.
271 1f). Likewise, we find that this cluster expresses *Platynereis piwi* (Fig. 1g), a key member of
272 the GMP [19], and *myc* (Fig. 1h), both of which are expressed in *Platynereis* PSCs [18]. These data
273 suggest that cluster 0 is a source of ectodermal PSCs.
274
275 As outlined above, *hox3* is preferentially expressed in ectoderm-derived PSCs. However,
276 additional populations of stem cells contributing to *Platynereis* growth and regeneration
277 have previously been hypothesized, including mesoderm-derived PSCs [21,42]. We therefore
278 systematically queried our single-cell atlas with a combined signature of stem cells (*piwi*,
279 *vasa*, *nanos*), proliferation (*proliferating cell nuclear antigen/pcna*) and chromatin remodeling
280 (*dnmt1*, *chd1*) These genes are expressed in cells of post-injury timepoints within several
281 clusters, hinting at additional sources of PSCs (Fig. 1g-h, Supplementary Fig. 3b-f).
282
283 To identify the most stem-like cells in each cluster in an unbiased, systematic way, we used
284 CytoTRACE, a computational method which assigns cells a score representative of their
285 "developmental potential", a proxy for stemness [43]. Cells were ranked by their CytoTRACE
286 score (within each cluster), and genes correlated with this score were calculated. This
287 analysis provides an unbiased, systematic overview of transcriptional changes within each
288 cell population as cells acquire a higher degree of developmental potential (Supplementary
289 data 4). We further determined gene ontology (GO) terms associated with the transcriptional
290 changes within each cluster, providing a more comprehensive resource for the involved
291 biological processes (Fig. 1i; Supplementary Data 4 and below).
292
293 As an additional approach to identify potential stem cells, we took advantage of the
294 observation that *Platynereis* PSCs exhibit larger nuclei and nucleoli [18,23], a feature usually
295 associated with increased transcriptional (and translational) activity [44]. Increased, broad
296 transcription, referred to as "hypertranscription", is frequently observed in active stem cells
297 and progenitors, closely associated with proliferation, and plays a role in stem cell activation
298 and function during growth and regeneration. Recently, absolute scaling of single cell
299 transcriptomes using Unique Molecular Identifier (UMI)-based sequencing data has been
300 shown to identify hypertranscriptomic stem cells and progenitors [45]. We therefore
301 investigated the dynamic changes in transcriptional activity upon injury in our dataset and
302 found evidence for hypertranscription (increased numbers of total UMIs detected per cell)
303 (Fig. 1j). Our analysis shows that there is a progressive increase in high-UMI cells during
304 regeneration (Supplementary Fig. 3g). Hypertranscriptomic cells are located within hotspots

305 of GMP-related gene expression and high CytoTRACE values on the UMAP (Fig. 1i) and can
306 be found in several clusters. Our analysis also revealed a sub-population of smooth muscle
307 cells showing high CytoTRACE values and piwi expression even before injury (cluster 12,
308 Figure 1b,g,ii), which could imply the existence of a dedicated progenitor state within this
309 specific tissue.
310
311 Taken together, we found several features associated with stem cells and the SAZ in injury-
312 adjacent cells. These features are predominantly detected after injury, increasing as posterior
313 regeneration proceeds. We found cells that strongly display these features distributed
314 among multiple, but not all clusters in this dataset, indicating multiple different sources of
315 regenerating PSCs.
316 To understand these putative sub-populations of the regenerated SAZ, and their cellular
317 origins, we focused our analysis on two major cell populations (clusters 0 and 1), which show
318 a strong activation of stem-cell-related features as described above.
319
320 To characterize these populations, we identified strongly expressed marker genes and
321 performed *in situ* Hybridisation Chain Reactions (HCR, see Methods and Supplementary Data
322 5) to detect their expression in the tissue. [16,46]. Co-labeling of both genes in posterior parts
323 of uninjured, posteriorly growing animals revealed that they demarcate two spatially distinct
324 tissues, corresponding to the ectodermal epidermis (cluster 0) and a sub-epidermal
325 mesodermal cell type (cluster 1) (Fig. 2a-e). The latter population covers the sub-epidermal
326 region, but does not include muscle. We therefore refer to this population as coelomic
327 mesoderm.

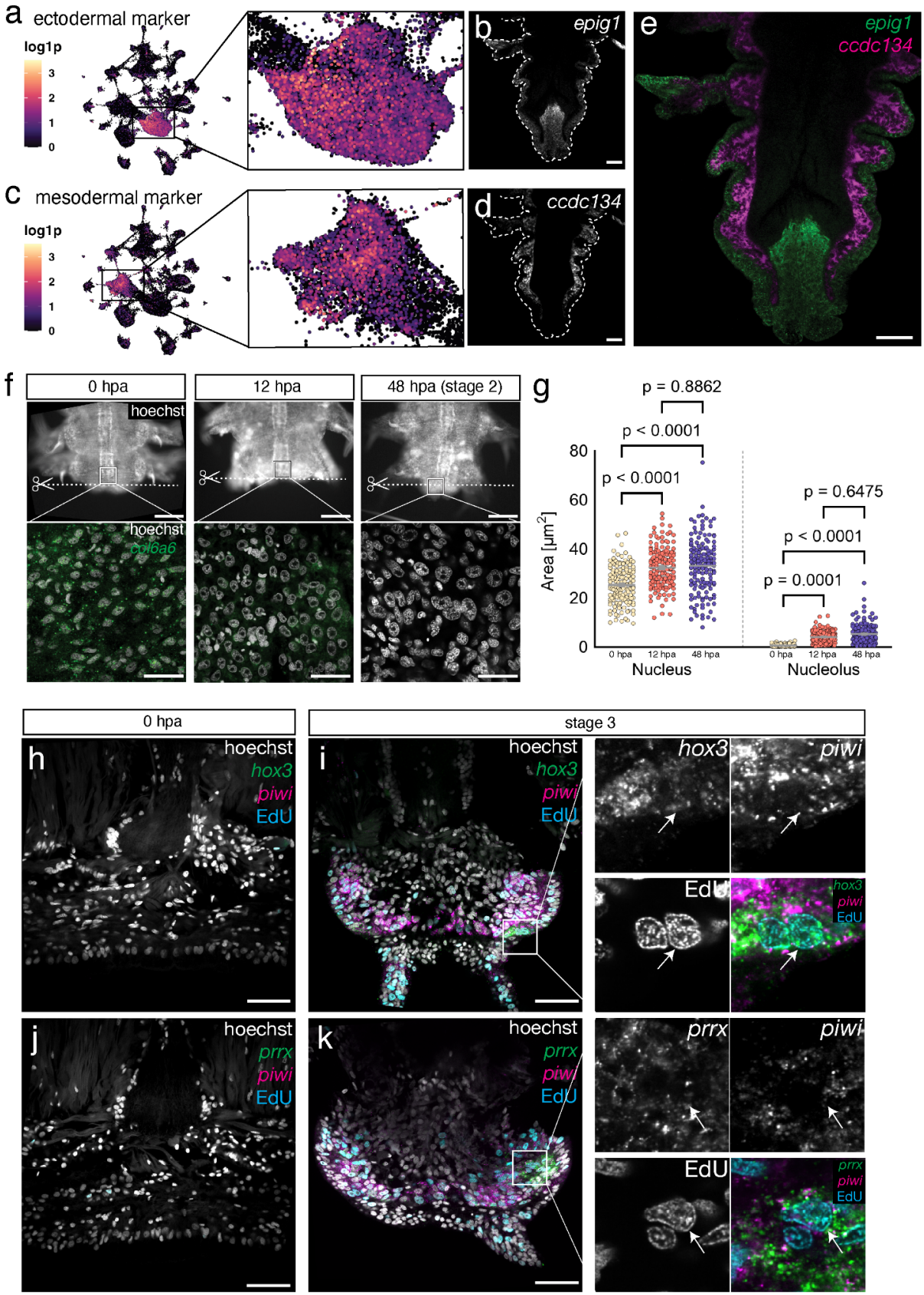

Figure 2. Distinct wound-adjacent cell populations acquire stem cell properties upon amputation.
(a,c) UMAP visualization of markers specific to cluster 0 (*epig1*) and 1 (*ccdc134*). (**b,d,e**) *in situ* HCR (uninjured animal, posterior end), showing mutually exclusive expression of *epig1* and *ccdc134* in the epidermis and coelomic mesoderm, respectively. Scale bar = 50µm. (f) Nuclear staining and *in situ* HCR of *col6a6* expression in wound-adjacent epidermal tissue at 3 timepoints after

posterior amputation. Amputation plane indicated with dotted line. Scale bar upper panels = 250µm, lower panels = 25µm. (g) Quantification of nuclear and nucleolar size change in regenerating tissue at 0, 12 and 48 hpa; each timepoint represents 3 individuals with 50 nuclei or corresponding nucleoli per individual. Statistical significance was calculated using a one-way ANOVA test with multiple comparisons. (h) *In situ* HCR of regenerating tissue at 0 and 72 hpa (stage 3), showing the expression of putative stem cell markers for ectodermal (*hox3*) and mesodermal (*prrx*), combined with a ubiquitous stem cell marker (*piwi*) and a proliferation label (EdU, 30min pulse before fixation); Scalebar = 50µm.

PSCs of ecto- and mesodermal origin exhibit shared and distinct molecular signatures

Having found evidence for distinct sources of regenerated PSCs, we next aimed to molecularly characterize them and profile them *in situ*. If indeed multiple populations of wound-adjacent cells acquire stem cell properties and repopulate the regenerating SAZ, our *in silico* data allows us to make certain testable predictions:

First, we examined whether cells of somatic origin change towards a teloblast-like morphology. As described above, *Platynereis* PSCs display a unique morphology with notably increased nuclear and nucleolar sizes. To test whether cells of this morphology emerge in wound-adjacent tissue, we stained tissue of posteriorly amputated *Platynereis* worms for the expression of *collagen alpha 6(VI) chain* (*col6a6*). Based on our CytoTRACE calculation, *col6a6* is strongly expressed in epidermal cells (cluster 0) and progressively lost as they acquire PSC-like properties (Supplementary data 4). Quantifying the surface area of nuclei and nucleoli in this population during regeneration showed a strong increase in both metrics after injury (Fig, 2f,g; Supplementary Fig. 4a-c), along with a gradual reduction of *col6a6* levels. These data are consistent with the gradual acquisition of a teloblast-like morphology.

Next, we reasoned that if these PSC-like sub-populations are distinct from each other, we should be able to find genes specifically enriched in either of them and should find their expression in distinct groups of cells *in situ*. As mentioned above, *hox3* has previously been described as a marker predominantly expressed in ectoderm-derived PSCs, and accordingly is mostly restricted to the PSCs we identified among epidermal cells (cluster 0). Based on this observation, we sub-clustered cells of both the epidermal (cluster 0) and the coelomic mesodermal (cluster 1) populations to define their respective PSC-like sub-populations. We used CytoTRACE-scores, the total number of UMIs and the expression of GMP, SAZ, proliferation and epigenetic remodeling-related genes to identify the respective subclusters (Supplementary Fig. 4) and discovered novel molecular markers unique to these cells (Supplementary data 3; Supplementary Fig. 4d-f, 5a-s). These new markers include genes encoding putative receptors, as well as proteins with DNA binding motifs such as transcription factors, thus establishing a set of molecules with possible regulatory functions (Supplementary Data 3).

For ectoderm-derived PSCs, our analysis not only identifies the previously described genes *hox3* and *evenskipped (evx)* but adds markers such as a *gene encoding a fibronectin leucine-rich transmembrane protein of unclear orthology (flrtl,* Supplementary Fig. 6f-j) and a gene (*sp/btd*) encoding the *Platynereis* homolog of the transcription factor Sp9 [47]. This population of cells further expresses early neuronal progenitor genes and patterning factors, such as the transcription factor gene *soxb1* (Supplementary Data 6) and the gene *four-jointed* that is involved in planar cell polarity, and was previously demonstrated to be expressed in developing medial neuroectoderm [36]. These data are consistent with the concept that these cells are the source of new neurons in post-regenerative growth.

For the mesoderm-derived population of PSCs, our analysis also predicts distinct marker genes. These include the gene *chd3/4/5b* that encodes a chromodomain helicase DNA-binding protein, and has previously been detected in regenerating mesoderm [24], as well as a gene we identify as *Platynereis paired-related homeobox* gene (*prrx*) (Fig. 2j,k, Supplementary Data 6; Supplementary Fig. 6k-o). The putative purinoreceptor gene *p2x* (Fig. 2i) and the *Platynereis* orthologue of the mesoderm related homeobox factor *msx* [48,49] are also predicted to be expressed in mesoderm-derived PSCs, albeit less exclusively than *prrx* (Supplementary Fig. 6k-t; Supplementary Data 3).

If *prrx* and *flrtl* are novel markers of distinct populations of stem cells, they should be expressed in separate, injury-adjacent populations of cells and exhibit morphological and molecular properties of stem cells. To test this prediction, we designed specific *in situ* HCR probes (Supplementary Data 5) and used these to analyze the expression of both genes in posterior regenerates (Fig. 2j,k; Supplementary Fig. 4d,e; whole-mount *in situ* hybridisation in Supplementary Fig. 4e). In agreement with our digital data, *flrtl* transcripts were co-expressed with *hox3* in cells of the epidermal layer, both at stage 1 and 3 (Supplementary Fig. 4d). By contrast, the predicted mesodermal stem cell marker *prrx* labeled cells at a deeper layer (Fig. 2j; Supplementary Fig. 4d). Consistent with the time-resolved atlas (Supplementary Fig. 6k-o), *prrx* was not yet detectable at stage 1 (Fig. 2l), but from stage 2 on (Fig. 2p). In both cases, a subset of labeled cells shows enlarged nucleoli as described for PSCs (arrowheads in Fig. 2h-k).

These sub-populations, based on our *in silico* data and their putative identity as stem cells, are predicted to be proliferating and expressing GMP genes. We therefore co-stained markers for ectoderm (*hox3*) and mesoderm (*prrx*) derived putative stem cells with the proliferation marker EdU and the key GMP factor *piwi*. We found both markers expressed in proliferating, *piwi* positive cells with teloblast-like morphology (Fig. 2h-j).

411 Taken together, these results are consistent with the notion that, during regeneration, distinct
412 populations of PSCs of mesodermal and ectodermal origin derive from existing cells not
413 displaying any stem cell related properties prior to injury. Our single-cell atlas allows the
414 identification of novel markers of these cells.

415 Clonal analysis by mosaic transgenesis reveals germ-layer 416 based lineage restriction of posterior growth and regeneration

417 Whereas our data argued for PSCs of distinct ecto- and mesodermal origin in the blastema,
418 it still remained unclear if these cells had identical potency, contributing to derivatives in all
419 of the regenerate, or if they were more restricted in their developmental potential. We
420 therefore turned towards a transgenic strategy that would allow us to address this question
421 at least on the broad level of germ layers.
422
423 Several other lines of evidence from previous studies suggest the existence of lineage-
424 restricted ectodermal and mesodermal stem cells during larval and juvenile posterior growth
425 in *Platynereis* [18,50–52]. The early embryogenesis of *Platynereis* follows a stereotypical
426 programme known as spiral cleavage [53,54]. Highly asymmetric cell divisions (unequal
427 cleavage) in the early embryo produce blastomeres of characteristic sizes and positions,
428 whose fate are strictly determined [50]. Micro-injection of a fluorescent lineage-tracing dye in
429 individual blastomeres at the earliest stages of the spiral cleavage process, shows that
430 ectodermal, mesodermal, and endodermal trunk tissues of the 4-day, three segmented larva
431 are produced, respectively, by micromere 2d, micromere 4d, and the macromeres 4A-4D of
432 the early embryo [50]. In another study, individual cells were tracked via live imaging from early
433 embryogenesis into early larval stages to identify the fates of the mesodermal 4d blastomere
434 [52]. This work revealed that the mesodermal bands and the primordial germ cells are produced
435 by asymmetric divisions of the 4d lineage. In addition, the final divisions of the lineage during
436 embryogenesis forms a group of undifferentiated cells at the posterior end of the hatched
437 larvae, which will possibly become the mesodermal PSCs in later stages. Due to the transient
438 nature of the signal (mRNA or dye injections), tracking the fate of putative PSCs into later
439 juvenile stages was not feasible. However, molecular profiling [18] suggests but does not
440 demonstrate the existence of at least two pools of PSCs with specific signatures, ectodermal
441 and mesodermal, organized as two concentric rings anterior to the pygidium, the terminal
442 piece of the *Platynereis* trunk (Supplementary Data 7, part A). So far, no transgenic lineage
443 tracing technique has been used to clarify the origin of tissues in the posteriorly growing or
444 regenerating juvenile.
445
446 To address this gap, we devised a mosaic transgenesis strategy using previously-established
447 Tol2 transgenesis methods [15]. We constructed a Tol2 transgenesis construct with a nuclear
448 mCherry and a membrane EGFP [52], under the control of the ribosomal protein rps9 promoter

449 for ubiquitous expression [15] (Fig. 3a). We injected several batches of zygotes at the one-cell
450 stage with the donor plasmid containing rps9::H2A:mCherry:F2A:mGFP transgene and
451 transposase mRNA. These G0 worms typically show mosaic integration of the transgene.
452 We raised the G0 batches that showed high numbers of surviving juveniles (Supplementary
453 Data 7) (Fig. 3b-j). To screen these individuals for fluorescence patterns and identify which
454 clonal lineages had the transgene integration, we amputated juvenile worms when they
455 reached 6 weeks. These original tails (pygidium + a few growing segments) were imaged via
456 confocal microscopy from both the dorsal and ventral sides. The amputated worms were
457 further raised in individual containers and allowed to regenerate their posterior parts for
458 three weeks. They were then amputated again one segment anterior to the regenerated part
459 to collect the regenerated posterior parts for imaging. The whole cycle was repeated once.
460 For each transgenic individual, we thus collected pictures of the primary clones derived from
461 transgenic blastomeres as a result of normal development, as well as pictures of two
462 reiterative, independent regeneration events from the same primary clones originating from
463 the non-regenerated trunk (Supplementary Data 7, part B).

464

465

466

467

468

469

470

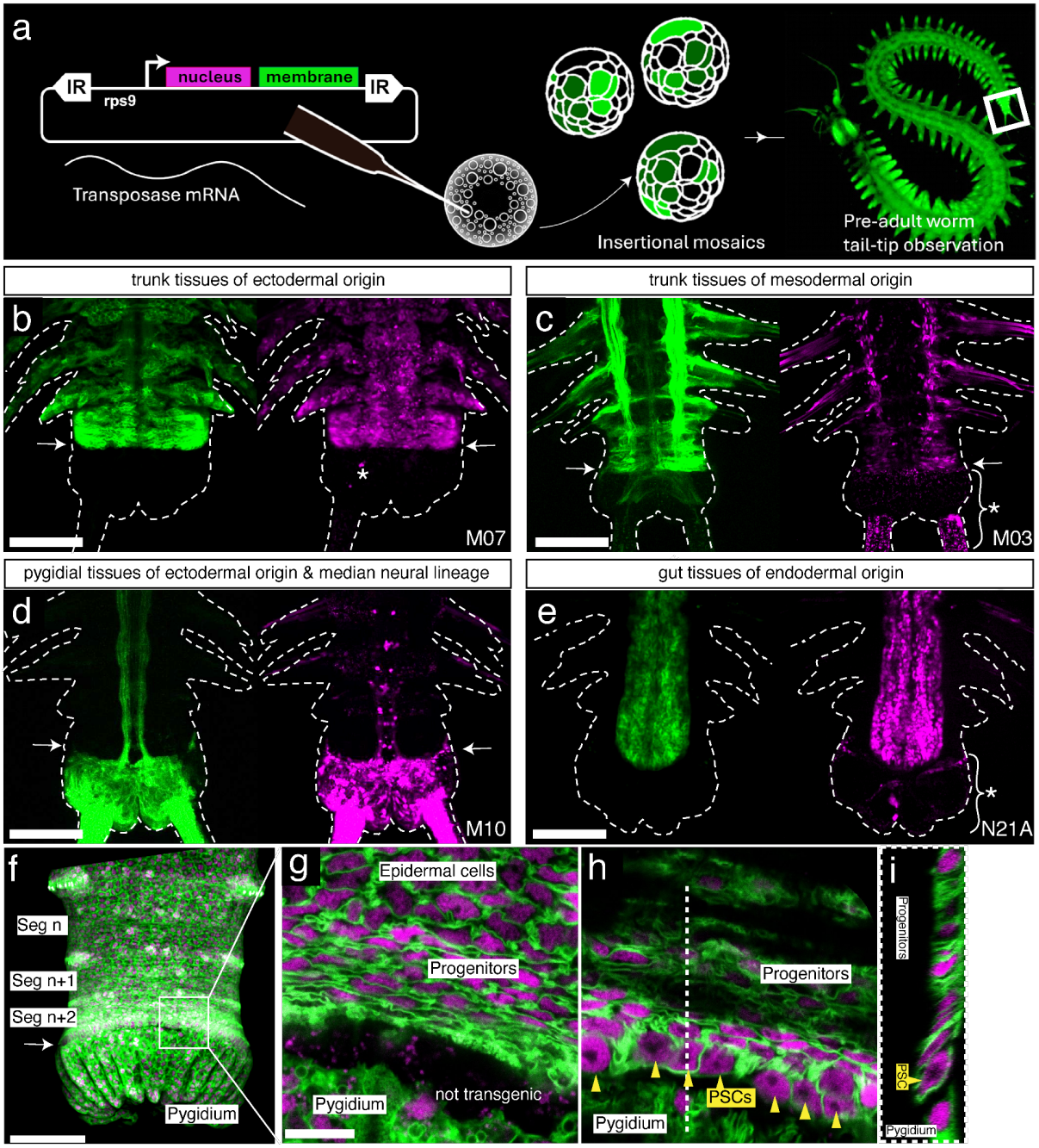

Figure 3. Mosaic transgenesis reveals developmental compartment-restrictions of PSCs in *Platynereis* posterior elongation. **(a)** Summary sketch of the protocol for creating large embryonic clones with transposase. **(b-g)** Examples of simple germ layer– or tissue-specific primary clones observed on posteriorly growing worms; 6 weeks, ventral views . **(b)** Ectodermal clone, no pygidial or internal cell labeled. **(c)** Mesodermal clone, only the muscles are clearly visible **(d)** Pygidial and median neural lineage clones. Most median neurites are emanating from pygidial sensory neurons. **(e)** Endodermal clone. **(f-i)** Dorsal views of a primary clone in ectoderm-derived PSCs. **(f)** General confocal stack projection, showing the position of the ectoderm-derived PSCs and uniformly labeled nascent segments; the pygidium is labeled with independent clones. **(g-i)** Magnified confocal section views of the SAZ region, at 2 µm z-depth **(g)**, 6.5 µm z-depth **(h)** and and y-z section **(i)**. **(g-i)** show the continuity of the clonal expression of the transgene in bottleneck-shaped ectoderm-derived PSCs with large nuclei-nucleoli (yellow arrowheads), transversely elongated columnar progenitor cells and squamous epidermal differentiated cells. For all panels, green labelings are cell membranes, magenta labelings are cell nuclei. White arrows: position of the PSCs. White asterisks: background staining. Scale bars: b-f: 100 µm; g-i: 10 µm.

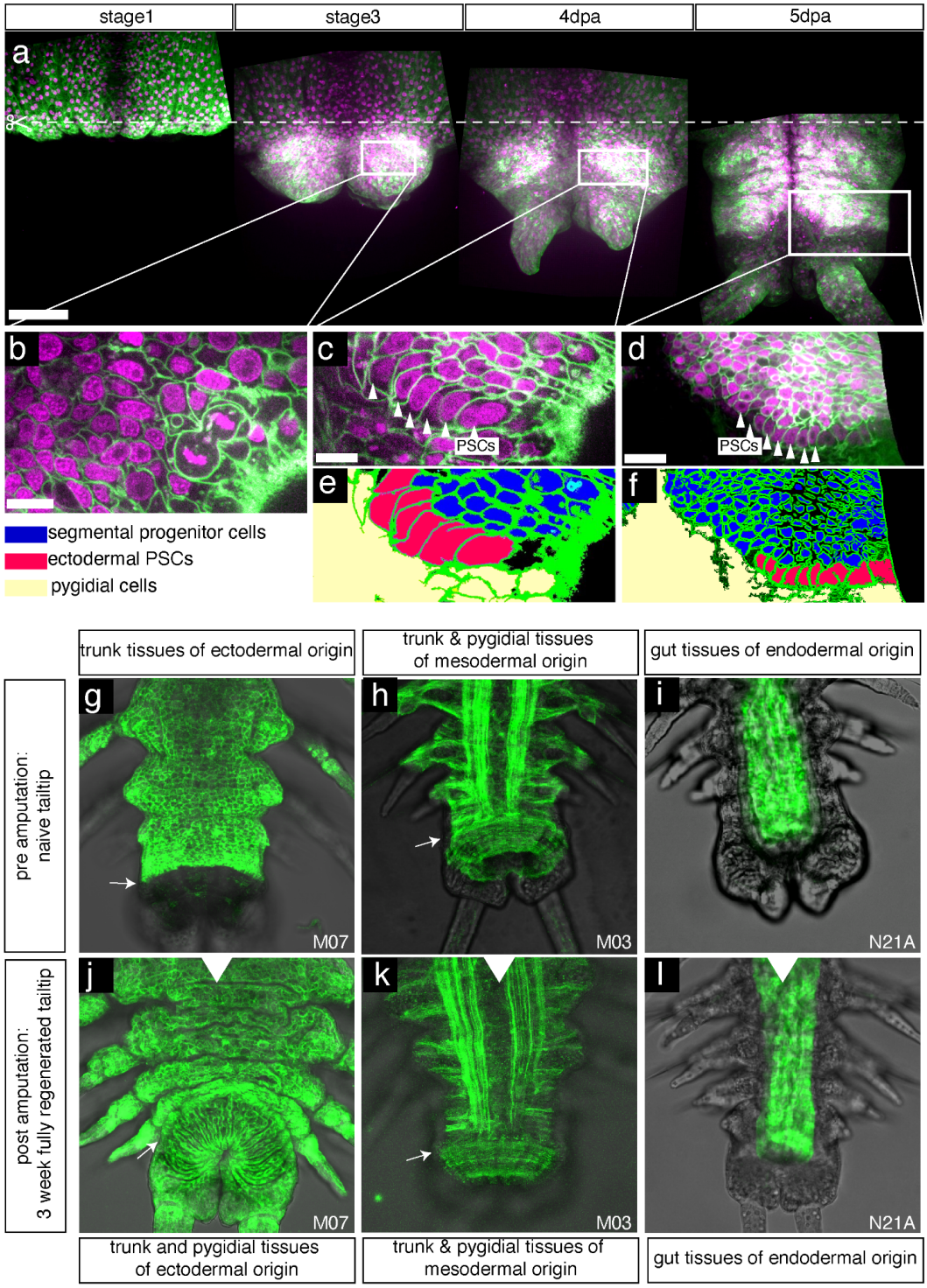

Figure 4. Persistent labeling of cells within developmental compartments during regeneration. (a) Time lapse ventral confocal stack projections of the regenerating tail tip of a worm displaying clonal transgene expression in the ectodermal lineage. (b-d) magnified confocal sections of the same individual. (e-f) interpretative schemes of (c-d). The time-lapsed views illustrate the continuity of clonal expression of the transgene in epidermal cells (a, stage 1), undifferentiated blastema cells (b), regenerated PSCs (c-d) and progenitor cells (c-d). (g-l) Regeneration experiments on animals bearing simple clones. Dorsal views of confocal stack projections, with pre-amputation views on top and the matching full regenerates (3 weeks post amputation) on the bottom. This series illustrates the strict compartment restriction in the regeneration of ectoderm-derived and mesoderm-derived PSCs, as well as gut endodermal lineage. Pygidial ectoderm, entirely removed upon amputation, is regenerated exclusively from trunk ectoderm precursors **(g, j)**. For all panels, green labelings are cell membranes, magenta labelings are cell nuclei. White arrows: position of rings of PSCs in the respective focal plane. Scale bars: a, 100 µm; b-c: 10 µm; d: 20 µm.

496 Overall, we found that most individuals showed complex patterns of fluorescent primary
497 clones. Although we cannot exclude that some of the patterns observed may be due to
498 enhancer trapping, we see no indication that this phenomenon occurs significantly in our
499 complete set of 61 transgenic individuals, presumably due to the relative strength of the
500 ubiquitous promoter we have used (*rps9*). All six individual primary clonal patterns we
501 deduce from observations are obtained multiple times (from 4 to 53 times, in 61 individuals,
502 Supplementary Data 7, part C), practically excluding that they may be due to neighboring
503 endogenous enhancers. The complexity of patterns likely results from a combination of
504 reasons: Firstly, multiple blastomeres were transformed (Supplementary Data 7, part B, N09
505 and N35 for examples) resulting in combinations of tissues labeled. Secondly, only a part of
506 a germ layer-derived tissue may be labeled. This is most evident in cases where only a
507 bilateral half of the tissues is fluorescent because transgenesis happened in only one of the
508 bilateral descendants of the germ layer founding blastomere (e.g. 4d divides bilaterally to
509 give the precursors of the right and left mesoderm, Supplementary Data 7 part B, M24 and
510 N23). Thirdly, some tissues were labeled in a stochastic, salt-and-pepper manner. This
511 phenomenon is known as variegation [55] and presumably happens when a transgene is
512 inserted near or within a heterochromatic region that imposes unstable transcriptional
513 repression on it. This was particularly recurrent at the level of ectodermal tissues
514 (Supplementary Data 7, part B, N25 and N33 for examples).
515
516 Despite this complexity, simpler patterns were also recovered in several individuals
517 corresponding to the labeling of the whole trunk ectodermal tissues (Fig. 3b), the whole trunk
518 mesodermal tissues (Fig. 3c) and the entire gut endoderm (Fig. 3e). The clonal nature of the
519 ectodermal patterns is indicated by the continuity of expression of the transgene in PSCs,
520 segmental precursors and differentiated segmental cells (Fig. 3f-3i). Ectodermal PSCs,
521 corresponding in location and cytological characteristics to the ring of cells identified by
522 molecular signature before (Gazave et al, 2013), are easily identifiable (Fig. 3h). Potential
523 mesodermal PSCs are also tentatively imaged in locations already identified molecularly
524 (Supplementary data 7, part B, M03). These primary clones support the aforementioned
525 concept that separate pools of precursor cells generate these sets of tissues during the life-
526 long process of posterior addition of segments. As for the endoderm, so far, no endodermal
527 PSCs have been identified by molecular signature, and it is possible that endodermal
528 precursors or stem cells are spread in a diffuse way along the length of the trunk [56].
529
530 In addition to the trunk germ layer-derived tissues, several primary clonal patterns were
531 obtained repeatedly either alone or in combination with others (Supplementary Data 7). The
532 pygidial ectoderm was often labeled independently of the trunk ectoderm (Fig. 3d). This
533 demonstrates that the pygidial ectoderm is derived from blastomeres different from the trunk
534 ectoderm and that the anterior border of the pygidial ectoderm with the trunk ectoderm is a
535 compartment border with no contribution of the pygidial cells to the growth of the trunk

536 ectoderm (Fig. 3b, d). The one exception to the pygidium/trunk compartmentalization is the
537 presence of a median neural lineage (Fig. 3d), composed of two pairs of cells per new
538 segment, that is also identified alone, sometimes unilaterally (Supplementary Data 7, part B,
539 M09, M10, N04, N11, N14, N26, N40 and O15). These cells are probably produced by
540 independent median specialized posterior stem cells that segregate from the 2d lineage in
541 the early embryo. Lastly, a lineage of amoeboid, presumably phagocytic cells, possibly
542 derived from anterior embryonic mesoderm, was observed several times (Supplementary
543 Data 7, part B, M09, N03, N05, N22).
544
545 Most importantly, germ-layer compartmentalization is fully conserved during regenerative
546 events (Fig. 4), with each germ layer of the regenerate originating exclusively from cells of
547 its kind in the neighboring non-regenerated trunk. The clonal nature of the transgene
548 expression is again illustrated by the continuous transgene expression in the differentiated
549 epidermal cells, blastemal cells, and the regenerated PSCs (Fig. 4a-f). Ectodermal
550 regenerated PSCs are clearly identifiable as soon as 4 days post amputation (Fig. 4c-d).
551 Lineage restrictions in the regeneration blastema (Fig. 4g-l) are in agreement with the distinct
552 source populations of stem cells suggested by our scRNAseq analyses. A diagram of the
553 whole set of primary clones obtained fully supports this interpretation of
554 compartmentalization (Supplementary Data 7, part C).
555
556 While these transgenic clones do not demonstrate the embryonic germ layer origins, they
557 show that tissues remain strictly compartmentalized during posterior segment addition,
558 similar to embryonic/larval development. Taken together, all these results are compatible
559 with the presence of the two rings of ectodermal and mesodermal PSCs immediately anterior
560 to the pygidium/trunk border, while the unsegmented endoderm may grow diffusely or
561 through the activity of specific endodermal PSCs yet to be identified. After amputation (which
562 removes all PSCs), ectodermal and mesodermal PSCs, as well as endoderm, are regenerated
563 exclusively from precursors of their kind in the uncut segments, either from dedifferentiating
564 cells, or from unknown resident lineage restricted precursor cells, in complete agreement
565 with the single-cell transcriptomics clustering.

566 TOR signaling is required for successful activation of PSCs and 567 regeneration

568 The protein kinase Target Of Rapamycin (TOR) has been implied in wound response and
569 blastemal signaling in planarians, zebrafish and axolotl [57–61], reviewed in [62]. Our *in silico*
570 analysis revealed increased expression of TOR- related transcripts in cells as they acquire
571 PSC identity in response to injury in *Platynereis* (Supplementary Data 4). These include the
572 *Platynereis* orthologs of genes encoding TOR (Supplementary Data 6) as well as
573 components of the ragulator complex (lamtor 1, 2, 3, 4 and 5), which is involved in TOR

complex activation and localisation, and therefore might influence cell metabolism and proliferation [63]. Additionally, many biological processes known to be controlled by TOR activity were found enriched in our GO-term analysis of genes associated with high CytoTRACE scores (e.g. translation, rRNA processing, ribosome biogenesis, see Supplementary data 4).

Moreover, increased TOR signaling has also been observed in hypertranscriptomic cells [45], as we observe them in the *Platynereis* regeneration process, and TOR complex activity has been shown to be a key requirement for maintaining a hypertranscriptomic state in embryonic stem cells [64]. We therefore investigated whether posterior regeneration in *Platynereis dumerilii* also required a functional TOR signaling system.

In our single-cell atlas, *Platynereis tor* was broadly expressed, including in the tentative PSC subpopulations (Fig. 5a-c). To assess whether or not TOR signaling was required for regenerating PSCs after amputation, we treated amputated animals with the ATP competitive TOR inhibitor AZD8055 [65] and compared their regenerative success to DMSO-treated controls (Fig. 5d-l). Already at 24 hpa, so before the formation of a significant blastema or a strong increase in cell proliferation [21], *in situ* HCR revealed that *myc* expression was strongly reduced and *hox3* expression was completely undetectable in treated animals (Fig. 5e,f), whereas control animals successfully established a zone of *myc*$^+$ and *hox3*$^+$ cells (Fig. 5i,j). Additionally, treated animals did not reach a stage 3 regenerate at 72 hpa (Fig. 5g,h). DMSO-treated control animals progressed normally and regenerated a blastema and early developing anal cirri within the same timespan (Fig. 5k,l). We therefore conclude that, upon TOR inhibition, *Platynereis* fails to regenerate PSCs, and subsequently does not develop a blastema or differentiated posterior tissues.

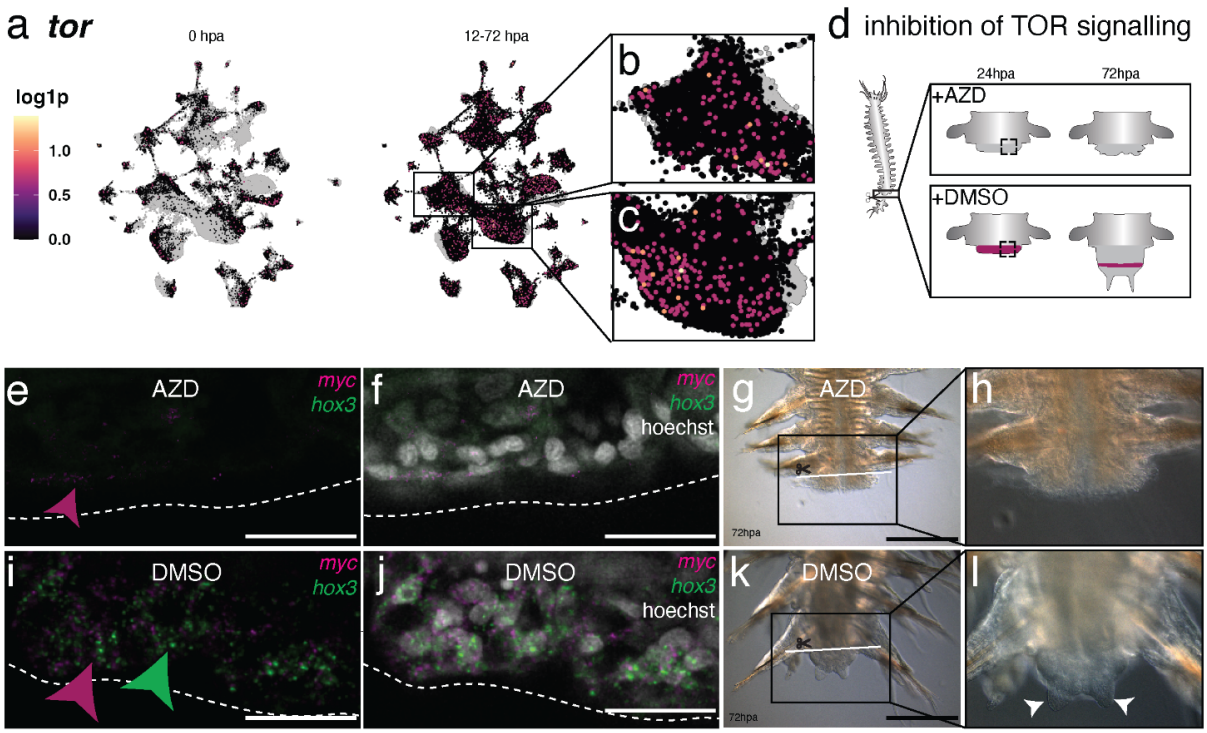

Figure 5. TOR signaling is necessary for re-establishing stem cell gene expression profiles and morphological regeneration upon injury.

(a-c) UMAP visualization of *tor* expression; (**a**) comparison between 0 hpa and 12-72 hpa; (**b,c**) enlarged views of cluster 0 and cluster 1 in 12-72 hpa samples. **(d)** Scheme of posterior amputation, TOR inhibition and posterior regeneration after 24 and 72 hours, highlighting region used for assessing stem cell gene expression 24 hpa. **(e-h)** Analysis of amputated animals (n=6) treated with AZD8055 TOR inhibitor. (**e,f**) Confocal images of *in situ* HCR stainings detecting expression of *hox3* and *myc* at 24 hpa; (**g,h**) brightfield images at 72 hpa; **(i-l)**. Equivalent analyses in DMSO-treated controls. (**i,j**) Confocal images of *in situ* HCR stainings for *hox3* and *myc* at 24 hpa; (**k,l**) brightfield images of posterior regenerates at 72 hpa. Scale bars: 25 µm (**e,f,i,j**); 250 µm (**g,h,k,l**).

Discussion

As outlined above, our work is consistent with the classical proposal that formation of the regenerative blastema of *Platynereis dumerilii* involves a process of injury-induced "re-embryonalisation" of wound-adjacent cells [23]. We advance this model to cell-type resolution, find molecular similarities to vertebrate blastema formation and present a clonal analysis furthering our understanding of lineage restriction during this process. Our data are consistent with both morphallactic repatterning processes and multiple parallel dedifferentiation events, and provide the molecular fingerprint of distinct groups of stem cells in posterior regeneration. These findings complement observations based on candidate genes and transcriptomic analyses in *Platynereis* and other annelid systems [21,66], and offer a fresh perspective on fundamental regenerative processes.

Both our transcriptomic and clonal analyses argue that, unlike planarians that exhibit pluripotent stem cells capable of regenerating all cell types of the adult [67], *Platynereis* regeneration relies on cells with limited potency that respect the distinction between cells arising from different germ layers in development. In both of these spiralian species, however, there appears to be a continuity of potency mechanisms between normal growth and regeneration processes: In planarians, pluripotent neoblasts are not only relevant for regeneration, but also homeostasis and growth [68]. Likewise, in *Platynereis*, lineage restriction applies to transverse growth, posterior growth, and regeneration. The dissimilarity of stem cell potencies within the clade of spiralians is reminiscent of the diversity of growth and regeneration mechanisms also found in cnidarians, where pluripotent stem cells are found in *Hydractinia* [69], whereas *Hydra* employs lineage-restricted progenitors [70]. As single-cell analyses in other annelid species are becoming available [66,71], we expect that the availability of time-resolved cellular and molecular data in the *Platynereis* model will help to more easily delineate differences and commonalities for regeneration-relevant stem cell mechanisms also in other spiralian species.

A recent single-cell study on the stem cell system in *Pristina leidyi* [71] found evidence for *piwi*-positive stem cells spread throughout the adult body of this annelid. The analysis identified a single, potentially pluripotent pool of stem cells at the root of all adult tissues. However, transcriptional heterogeneity was detected in this *piwi* positive population, and lineage-restriction could not be ruled out. Unlike *Platynereis*, *Pristina* reproduces by fission, and a large population of *piwi* positive cells was detected in a developing fission zone. As the experiments in *Pristina* were not conducted in a regeneration context, further experiments will be needed to allow direct comparisons of stem cell systems between these two more closely related species. Such comparisons could reveal important insights into the evolution of asexual reproduction and how it affects stem cell potency and availability.

As the labeled clones we obtain by zygotic injections are primarily large, they are well suited to provide a clear view of germ-layer-restricted lineages, but cannot yield experimental access to smaller lineages in both posterior growth and regeneration. Our single-cell transcriptomic atlas corroborates multiple distinct clusters of progenitors that are confined to individual germ layers, but also exhibit further subdivisions. It is thus possible that there are even more restricted lineage compartments currently not accessible to experimental validation. In turn, not every transgenically labeled compartment contributes to its regenerated counterpart. One example is the bilateral neural lineage that we identify, which is continuous with the pygidium before amputation, but does not visibly contribute to the regenerate. The existence of such a developmental compartment is consistent with the idea that there might be distinct subsets of *hox3*-positive PSCs in the ring-like segment addition zone, possibly reflecting the existence of distinct neurogenic columns in posterior growth [72]. More refined mapping techniques will be required to assess if such subsets exist in regular development, and if they are reconstituted in the process of regenerative growth.

Our data not only provide insight into the likely source and restriction of PSCs in *Platynereis* regeneration, but also into molecular factors involved in the emergence of blastemal cells and their possible conservation. Based on our findings and existing literature, we propose a working model of regeneration in *Platynereis* consisting of the activation and dedifferentiation of wound-adjacent cells, their acquisition of distinct, lineage restricted stem cell properties and ultimately their proliferation and contribution to regenerating tissue. While dedifferentiation as a source of blastemal stem cells in annelids has previously been proposed [8,10,20,21,23,25], we report cell-based molecular data consistent with this concept. We observed multiple distinct populations of cells responding in similar ways: they start expressing *myc* which, besides its general role in stem cell activity, has been shown to be involved in mammalian dedifferentiation and pluripotency [73,74], as well as several genes of the germline multipotency programme (e.g. *piwi*, *vasa*, *nanos*), which are also expressed in *Platynereis* PSCs during regular growth. These cells show hypertranscription, a known feature of active adult stem cells [44,45], strong expression of genes involved in epigenetic reprogramming (e.g. *chd3/4/5b*, *dnmt1*, *chd1*), and start to proliferate. Both *myc* and *chd1* have previously been shown to play a central role in stem cell activation and hypertranscription in many species, such as the endothelial to hematopoietic stem and progenitor transition in mouse development [44,75].

Together, these findings strengthen the argument for multiple, parallel dedifferentiation events underlying regeneration in *Platynereis*. Our data do not exclude the possibility that resident stem cells or dedicated progenitors among heterogeneous pools of differentiated cells could also contribute to the regenerate, as has been proposed or observed in multiple regeneration models including annelids [5,8,10]. Our findings of *piwi* expression and high CytoTRACE value in a subset of smooth muscle cells before injury might indicate the

688 existence of a progenitor-like cell state in this particular tissue. However, the fast *de novo*
689 establishment of the molecular stem cell signature within 12 to 24 hpa, before a detectable
690 increase in proliferation commences, argues that such a contribution may only account for a
691 limited set of blastemal cells, or specific tissues, as suggested for gut cells during
692 regeneration in a recent publication [76].
693
694 Apart from those more general processes involved in the regeneration programme, the
695 notion that PSCs resulting from epidermal and coelomic mesodermal cells are molecularly
696 distinct will also be helpful in more clearly delineating possible parallels to established,
697 dedifferentiation-based regeneration mechanisms in other systems. Indeed, the expression
698 of the *sp9* homologue *sp/btd* in epidermis-derived PSCs of *Platynereis* is reminiscent of the
699 expression of *sp9* in the dedifferentiating epidermis of axolotl blastemas [77]. In turn, similar to
700 the axolotl *msx-2* gene that becomes refined to the mesenchymal part of the blastema [78],
701 we identify its *Platynereis* ortholog *msx* to be present in the *bona fide* mesodermal PSC
702 clusters. Likewise, our work revealed a previously uncharacterized *Platynereis prrx1*
703 orthologue that is expressed in the mesodermal PSCs. Vertebrate *prrx1* genes are
704 prominently expressed in mesenchymal cells during limb development of chicken [79], and
705 mouse [80], and have also been characterized as part of the connective tissue progenitor cells
706 in axolotl and frog blastemas [22,78,81]. It has previously been argued that evolutionary
707 understanding of blastema-based regeneration will require a more detailed understanding
708 of the underlying genetic circuitry [3]. Our work establishes *Platynereis* as a promising
709 candidate for such analyses and provides a first comprehensive set of data towards this end.
710
711 The prevalent expression of ribosome- and cellular growth related genes in PSC-like cells
712 during regeneration warranted an investigation of the role of TOR signaling in the activation
713 or dedifferentiation or activity of stem cells in our model. As discussed above, TOR signaling
714 has previously been implied in regeneration in many species, with a recent article
715 demonstrating its crucial, regulatory role upstream of axolotl limb regeneration [57]. While the
716 exact role this pathway plays in this process is not well understood, its activity seems to be
717 generally required for regenerative stem cell proliferation. Interestingly, the formation of
718 stem cells through dedifferentiation occurs during a period of lower TOR activity and high
719 autophagy (which TOR usually inhibits) [62]. We found that impaired TOR signaling in
720 *Platynereis* not only affects proliferation and the morphological formation of a blastema, but
721 directly blocks the otherwise reliable establishment of PSCs as early as 24 hpa, suggesting
722 an early, central role of TOR kinase activity in regulating the dedifferentiation of cells in
723 response to injury.
724
725 Lastly, we expect our methodological advances presented in this manuscript to be of broader
726 use in the establishment of additional resources for comparative regeneration biology. Using
727 a widely applicable cell fixation method and parallel processing of all samples allowed us to

728 generate a merged, temporally resolved dataset without having to rely on computational
729 batch effect removal strategies. Similarly, whereas regular pre-processing would normalize
730 cellular transcriptomes to comparable levels, we suggest that the hypertranscriptomic state
731 of cells at later regenerative timepoints reflects a biological feature of PSCs. Finally, our
732 clonal analysis approach offers a direct way to observe clonogenic lineages in development
733 and regeneration as well as new insights into *Platynereis* lineage restriction, without
734 requiring stable expression of transgenic constructs beyond G0. Taken together, our
735 manuscript therefore provides a framework and methodological toolkit for future projects
736 aimed at acquiring and analyzing the data required to compare regeneration across species
737 and ultimately advance our understanding of blastema-based regeneration.

738

Methods

Animal culture

Platynereis dumerilii were kept in laboratory culture at temperatures between 18° and 20°C in a 16:8-hour light-5 dark (LD) cycle, and maintained under previously published conditions [17,82], adhering to the applicable national legislation.

Posterior amputation surgery

To perform posterior trunk amputation surgery, animals were anesthetized in 7.5% $MgCl_2$ diluted 1:1 with sea water. For bulk- and single cell transcriptomics and for all *in situ* HCR labelings shown, animals of 40-60 segments size and 3-6 months age showing no signs of sexual maturation and no prior injuries were sampled. Amputations were done by performing a transverse section posterior of segment 30, using surgical scalpels (Swann-Morton, Type 11). For regeneration time courses, animals were then rinsed in sea water and transferred to fresh culture boxes for recovery.

Bulk RNA sequencing of regenerating tissue

Posterior surgeries were performed as described above. Tissue was then harvested at each sampling time point by anesthetizing animals again as described above, followed by a transverse cut anterior of the wound-adjacent segment, right at the segment boundary. Tissue pieces were transferred to sea water, pooling 8 pieces per replicate, on ice. After tissue pieces sank to the bottom of the reaction tube, the supernatant was removed and the samples were frozen in liquid nitrogen and stored at -80° C.
RNA extractions were performed using a commercial kit (Direct-zol RNA MiniPrep, Zymo Research, USA), following the manufacturer's guidelines. RNA was eluted in 30 µl RNAse-free H2O. Illumina sequencing libraries were prepared at the Vienna Biocenter Next Generation Sequencing Facility, using NebNext Dual adaptors with dual indexing. Libraries were then sequenced using the Illumina NovaSeq platform with S1 PE100 flowcells.

Bulk RNA sequencing analysis

Sequences were trimmed using cutadapt (v. 1.12) [83] and analyzed for sequence quality using fastQC (v. 0.11.9) [84] and multiQC (v. 1.14) [85]. We used STAR aligner (v. 2.7.10b) [86] to generate a reference file from the *Platynereis* genome assembly draft (*genomeGenerate*) and align sequencing reads (*alignReads*), then extracted a counts matrix using featurecounts (v. 2.0.1) [87]. Data were then processed using DESeq2 (v. 1.36.0) [88] and mfuzz (v. 2.56.0) [89], estimating ideal clustering variable and cluster number following the software package guidelines. Cluster members (membership cutoff = 0.5) were then plotted using ggplot2 (v. 3.4.2) [90], with select genes of interest plotted in color (supplementary Fig. 1).

Single cell transcriptome sequencing

For single-cell RNA sequencing, we performed posterior amputations and regeneration time courses similar to those described above. However, after sampling the wound-adjacent segments, we transferred those to an acetic acid/ methanol (ACME) solution with 1% NAC for dissociation [27]. Cells were then dissociated over the course of 45 minutes, interspersed with rigorous pipetting every 15 minutes using a P1000 pipette pre-coated in 1% BSA in PBS to reduce cell loss due to stickiness. Dissociated cells were centrifuged (1000 g for 5 min at 4°C), resuspended in storage buffer (1% BSA in PBS, with 10% DMSO and 1U/µl recombinant RNAse inhibitor, Takara Bio) and stored at -20° C for further processing.

To remove debris and concentrate cells, we performed FACS on freshly thawed samples. We first labeled nuclei (Hoechst 33342 at 5 µg/ml, for 15 minutes at room temperature), then sorted 15,000 cells directly into 10X genomics chromium buffer, using FACS gates (FSC-A vs FSC-H; DAPI-A) to exclude debris and clumped cells (BD FACS Aria IIIu).

Single cell barcoding droplet (GEM) production and library preparation was performed at the Vienna BioCenter Next Generation Sequencing facility using the 10X genomics Chromium platform according to manufacturer's instructions (10X 3' v3 chemistry, 10X Dual Index Kit). Two independent experiments were performed (replicates a and b), following the same strategy: all animals for one experiment were sampled from sibling- or closely related batches of animals. Amputations were performed in parallel, and by freezing ACME-dissociated cells, we were able to store sampled cells throughout the regeneration time course. All samples were then sorted, and barcoded in parallel. Libraries were sequenced on the Illumina NovaSeq platform (S4 lanes, PE150).

Single cell data processing

We used Cellranger software by 10X genomics (v. 7.0.1) to generate a custom genome reference (*mkref* function) from the *Platynereis* genome (Genbank ID: GCA_026936325.1), using gene annotations provided in ref. 91. We then assigned reads to cellular barcodes, aligned them to the custom reference and generated a read barcode matrix for each sample individually using the *cellranger count* function with *expect-cells* set to 10000.

Our main processing pipeline was based on the "Seurat" package for R [92], with specific modifications for merging multiple datasets. In brief, we imported the barcode matrices (*Read10X* with min.cells = 3 and min.features = 200) and followed standard pre-processing steps. Outlier cells were removed based on manual inspection of scatterplots (counts vs features), removing between 30 and 108 cells per dataset. Quality metrics and cutoff values for all samples are available in (Supplementary Data 1).

We merged all datasets following an approach employed elsewhere [93]. We normalized the data (LogNormalize with scale.factor = 10000) and identified the variable features for each dataset individually (using FindVariableFeatures). We then used the union of all variable features from all different timepoints to conserve features which might be variable only at a

817 certain timepoint, and used this set of features for the merged dataset. Next we scaled the
818 merged dataset and performed dimensionality reduction (first 50 dimensions in PCA
819 space). We then calculated the UMAP embedding and performed cell-type clustering. After
820 trying multiple clustering resolutions we settled on a resolution of 0.5 as it best reflected
821 known biological cell types and subpopulations.
822
823 **Single cell cluster annotation**
824 Marker genes were identified for each cluster using the Seurat *FindAllMarkers* function
825 (only returning positive markers at a min.pct of 0.25 and a log-fold change threshold of 1).
826 As the reference genome used in this manuscript lacks a gene name annotation, we
827 annotated marker genes here and below using a table of best BLAST hits for each coding
828 sequence identified on the genome (see "transcriptome annotation" below). The annotated
829 table of markers for each cluster (Supplementary Data 3), combined with screening
830 expression of an array of genes with known expression patterns in *Platynereis*
831 (Supplementary Data 2) were then used to annotate the clusters.
832
833 **Bulk- and single cell sequencing data comparison**
834 For quality control, we correlated single cell and bulk RNA sequencing data. Due to the
835 differences in sequencing technologies, strong correlation is not necessarily expected.
836 However, mismatched correlation between bulk- and single cell timepoints might indicate
837 biological differences or technical issues. To this end, we extracted aggregate
838 ("pseudobulk") counts from the single cell dataset (grouped by timepoint) using the Seurat
839 AggregateExpression function. Bulk sequencing counts were extracted using the DESeq2
840 counts function. All counts were then subset to only contain features identified as variable
841 in the single cell object, expressed in at least one replicate in both bulk and single cell data.
842 We then scaled all remaining features by division by the sum of each feature's expression.
843 Pearson correlation was calculated using the cor function (stats package v4.3.3) with
844 default parameters and visualized using the pheatmap package (v1.0.12) function
845 pheatmap, also at default parameters.
846
847 **Single cell doublet prediction**
848 Potential cell doublets (2 or more cells assigned the same cellular barcode) were estimated
849 using the R package DoubletFinder (v2.0.3 - note that the latest version, 2.0.4., introduces a
850 code-breaking change)[29]. In brief, optimal parameters were determined and doublet scores
851 were calculated for each dataset independently. Expected number doublets based on fluid
852 dynamics in 10X Chromium devices was determined based on manufacturer instructions
853 (https://kb.10xgenomics.com/hc/en-us/articles/360059124751-Why-is-the-multiplet-rate-
854 different-for-the-Next-GEM-Single-Cell-3-LT-v3-1-assay-compared-to-other-single-cell-
855 applications), rounding to the closest available number. For doublet prediction, 30 principal
856 components and a pN value of 0.25 were used.

857
858 **Analysis of UMIs per cell**
859 UMI values of cells were compared between timepoints post amputation using the
860 Wilcoxon rank sum test with continuity correction (Supplementary. Fig. 3). To ensure these
861 results were not affected by outlier removal (see above), we performed the same test on
862 cells without removing outliers, yielding comparable results (0 hpa vs 24 hpa: $p < 2.2e-16$;
863 24 hpa vs 72 hpa: $p < 1.227e-11$).
864
865 **CytoTRACE analysis**
866 To rank cells by their developmental potential, we used CytoTRACE (v.0.0.3). CytoTRACE
867 is a statistical method, which uses transcriptional diversity as a proxy for developmental
868 potential and assigns a CytoTRACE-score to each cell [43]. CytoTRACE scores were
869 calculated for each cluster independently, using default parameters, then transferred to a
870 metadata slot of the Seurat object. Several biologically similar clusters were merged for
871 this analysis (3, 6 and 12; 4 and 16; 8 and 14). While CytoTRACE has been shown to work
872 on a broad range of datasets and organisms, we focussed our analysis on clusters in which
873 known biological information (e.g. expression of established stem cell marker genes) could
874 be used to assess its results. Data for all clusters is available (Supplementary data 4), and
875 validations (i.e. CytoTRACE score matching expression of stemness-related genes) were
876 performed for clusters 0 and 1.
877
878 **Gene annotation**
879 Top genes of every cluster were annotated using an automated pipeline. For this, all
880 transcript sequences predicted from a given gene locus (XLOC ID) were used for sequence
881 searches using BLASTX [94] against two protein databases: a version of the NCBI
882 Uniprot/Swissprot repository (accessed on June 16, 2021) and a database combining
883 entries of the more inclusive NCBI RefSeq repository (accessed on November 25, 2021).
884 For the latter one, all protein sequences available for a set of representative landmark
885 species and taxa were used: Annelida, the mollusks *Mytilus galloprovincialis, Crassostrea*
886 *gigas, Mizuhopecten yessoensis, Octopus bimaculoides, Pomacea canaliculata, Lymnaea*
887 *stagnalis, Biomphalaria glabrata, Aplysia californica*; the insects *Drosophila melanogaster,*
888 *Apis mellifera, Clunio marinus, Nasonia vitripennis*; and the chordates *Branchiostoma, Mus*
889 *musculus, Oryzias latipes, Danio rerio and Gallus gallus*. Best hits for each of these
890 searches were tabulated. For gene loci with multiple transcripts, the results for the
891 transcript that retrieved the highest score in the analyses was retained as reference, so that
892 each gene locus retrieved one annotation.
893
894 For investigation of specific genes, we assembled *bona fide* full length sequences
895 independently of the genome annotation, using available RNAseq data generated for the
896 laboratory strains (PIN, VIO) maintained in the laboratory [9]. Sequences from individual

libraries were assembled using the CLC Main Workbench Software package (version 23.0.2), and predicted protein sequences subjected to domain analysis using SMART [95]. Assembled gene sequences for *Platynereis prrx, flrtl, p2x, epig1, ccdc134, tor, lamtor1 to 5,* and *smg1* were submitted to the NCBI Genbank repository.

Gene Ontology Analysis

To assess the CytoTRACE-scores further and look for potentially informative associated gene expression patterns, we calculated Pearson-correlation values for each gene with the CytoTRACE score of each cluster, using the CytoTRACE software with default parameters [43]. We then ordered genes by this correlation and performed GO term enrichment analysis for each cluster using CERNO [96] as implemented in the tmod R-package (version 0.50.13) [97].

Pearson correlation scores with CytoTRACE scores were calculated for the full gene-set. Because GO terms are not annotated for *Platynereis*, we identified the closest matching human gene symbol (see "gene annotation" above, limited to human gene hits) and translated these to entrez-ids for GO term analysis. Therefore, this analysis exclusively focuses on genes with a close human orthologue. We then used the three human GO term annotation sets as accessible through the org.Hs.egGO R-package (version 3.17.0) and performed the CERNO enrichment test.

Phylogenetic analyses

For phylogenetic analyses of selected *Platynereis* proteins whose phylogeny was not yet previously reported, we used the following strategy: We identified the top hits in selected reference species representing key vertebrate phyla (mammals, birds, amphibians) as well as invertebrate phyla (mollusks, insects) by performing BLASTP searches against the NCBI clustered nr database. For identifying / completing matching sequences in the axolotl (*Ambystoma mexicanum*), we made use of the Axolotl-omics web resource (https://www.axolotl-omics.org/) that allowed access to the latest axolotl transcriptome assembly (AmexT_v47). Proteins were aligned using the CLC Main Workbench Software package (version 23.0.2) and cleaned of short sequences. Subsequently, alignments were exported and used for phylogenetic analyses using IQ-Tree 1.6.12 [98,99], allowing for the choice of the most suitable substitution model. Ultrafast bootstrap analysis [100] with 1000 repetitions was used to assess confidence for individual branches. The most likely tree topology was then visualized using the iTOL suite [101], available at https://itol.embl.de .

Sub-clustering populations with stem cell like properties

To identify markers specific to sub-populations of clusters with stem cell like properties, we subset clusters 0 and 1 (epidermis and coelomic mesoderm) and re-processed these

937 transcriptomes as described above, but without identifying variable features for each
938 sample individually. Newly calculated clusters were then analyzed for their expression of
939 GMP and SAZ related transcripts as well as their UMIs per cell. Strongly positive
940 subpopulations were identified for both clusters. Marker genes for those subpopulations
941 were then calculated against the entire dataset (suppl. Fig. 4, 5; full marker gene table in
942 Supplementary Data 3).
943
944 **Plotting and visualization**
945 All plots displaying single cell data were generated using the R package SCpubr (v. 1.1.2)
946 [102]. The displayed values on gene expression UMAPs are log-transformed transcript counts
947 normalized by UMI.
948
949 ***in situ* Hybridization Chain Reaction (HCR)**
950 For *in situ* visualization of gene expression, we sampled tissues of either growing or
951 regenerating animals as described above. Labeling was done following our previously
952 published protocol for *Platynereis* [16], with probes designed using the publicly available
953 algorithm HCR3.0 Probe Maker (v. 2021_0.3.2, described in ref. 103). All HCR probe
954 sequences are available (Supplementary Data 5).
955
956 **Whole Mount *In Situ* Hybridization (WMISH)**
957 The gene sequences for *Platynereis prrx* and *flrtl* were amplified by PCR on cDNA of stage
958 7 regenerates (7 days post amputation) and cloned into pJet2.1. Primers introducing an Sp6
959 promotor sequence were used to generate the transcription templates. Digoxigenin-labeled
960 probes were synthesized by Sp6 *in vitro* transcription, cleaned using the RNeasy Kit
961 (Quiagen) and stored in hybridisation mix at -20°C. Nitro blue tetrazolium chloride/5-
962 bromo-4-chloro-3'-indolyphosphate (NBT/BCIP) WMISH was performed as previously
963 described [104]. Samples were permeabilized with proteinase K for 45 seconds. Bright field
964 pictures for NBT/BCIP WMISH were taken on a Zeiss Z2 Imager, 20x objective.
965
966 <u>Primers to amplify gene sequences</u>
967 prrx_for: CGGAATTGCCTCAGCTTACTACTCTC
968 prrx_rev: CTGAGCCATCTGGTGGTGGTGG
969 flrtl_for: GTTCCCTTGCAGTCACTTT
970 flrtl_rev: CACTGTTCCTCTTGCCTTTT
971
972 <u>Primers to generate antisense probe template</u>
973 prrx_for: CGGAATTGCCTCAGCTTACTACTCTC
974 pJet2.1_sp6_rev: GGATTTAGGTGACACTATAGAACGACTCACTATAGGGAGAGCGGC
975 flrtl_for: GTTCCCTTGCAGTCACTTT
976 pJet2.1_sp6_rev: GGATTTAGGTGACACTATAGAACGACTCACTATAGGGAGAGCGGC

977
978 **Microscopy and image analysis**
979 Confocal images of *in situ* HCR labelings were taken using a Zeiss LSM700 confocal
980 microscope with a Plan-Apochromat 40x/1.3 Oil DIC, WD 0.21 mm lens, using Zeiss Zen
981 software. Images were then processed using FIJI software [105] for adjustment of contrast,
982 LUT selection and creation of overlay images.
983
984 **Quantification of nuclear and nucleolar size in regenerating tissue**
985 To quantify the change in nuclear and nucleolar size of cells responding to posterior injury
986 over time, animals at 0, 12 and 48 hpa were processed and imaged as described above.
987 Nuclei and nucleoli were manually selected as regions of interest (ROIs) in FIJI software by
988 drawing an outline around the areas positive for the nuclear stain (nucleus) and the roughly
989 circular areas within negative for the stain (nucleolus). 50 nuclei and corresponding nucleoli
990 closest to the amputation site were counted per biological replicate (n = 3 for each
991 timepoint); nuclei that did not fully span the focal plane were excluded from the analysis.
992 The data were plotted in GraphPad Prism v10.2.2, and the statistical significance of the
993 differences in means between the timepoints was calculated with a one-way ANOVA test
994 with multiple comparisons.
995
996 **Molecular Cloning**
997 The transgene rps9::H2A::mCherry::F2A::GFP::CAAX (simplified as pHCX) was engineered
998 using the Gibson assembly protocol [106]. The donor plasmids for this construction were
999 pEXPTol2-EGFP-CAAX, pEXPTol2-H2A-mCherry [52] and pTol2{rp-s9::egfp} [15]. The
1000 ribosome skip site coding sequence F2A was inserted between the two recombinant
1001 fluorescent protein coding sequences by adding it to the cloning primer. For the Gibson
1002 reaction, Gibson assembly master mix (NEB, France, E2611S) and NEB 5-alpha Competent
1003 E.coli (NEB C2987H) were used, following the manufacturer's protocol.
1004
1005 **Generation and analysis of transgenic animals**
1006 *Tol2* transposase mRNA was synthetized using the SP6 mMessage kit from Ambion
1007 (AM1340). The manufacturer's protocol was followed until the end of DNase step (1ml
1008 DNase 15 mins at 37°C). For purification of mRNA, MEGAclear kit from Ambion (AM1908)
1009 was used, following RNA elution option two with the following modifications: elution
1010 buffer was heated to 72°C, this warmed elution buffer was applied to filter cartridge
1011 containing mRNA, the tubes were kept at 72°C heated plate for 5 min before centrifuging
1012 for elution.
1013
1014 For micro-injections, previous protocols were used [52,107]. Briefly, fertilized eggs were
1015 dejellified at 45 mins post fertilization, using a 80 mm nylon mesh. The egg cuticle was
1016 softened with a flash treatment with proteinase K diluted in seawater (100 mg/ml). After

1017 abundant rinsing with sea water, the eggs were micro-injected with a mix of Tol2
1018 transposase mRNA (300 ng/ml) and plasmid pHCX (100 ng/ml). Injected eggs were
1019 incubated overnight at 28°C. Injected batches of larvae and juveniles were raised in a
1020 common polypropylene container with 800 ml of sea water until they reached 6 weeks.
1021 Worms were then relaxed and amputated as described before. Amputated posterior parts
1022 were kept in 7.5% $MgCl_2$ diluted 1:1 with sea water and mounted on slides using three
1023 layers of tapes as spacer. Confocal images were acquired on a Zeiss LSM 780 confocal
1024 scanning microscope. Amputated animals were dispatched in individual boxes and fed
1025 carefully to avoid fouling of the small amount of sea water. The operation was repeated
1026 twice after three weeks of regeneration. Some individuals however were not documented
1027 for two rounds of regeneration because they underwent sexual maturation, that stops
1028 regeneration.
1029
1030 **AZD8055 treatment**
1031 Animals were surgically amputated as described above. Regenerating animals were then
1032 kept in glass beakers in artificial sea water, either treated with 10μM AZD8055
1033 (MedChemExpress, USA) or with an equal amount of carrier control (DMSO).

1034

Data Availability

All primary data generated for this manuscript are available online. The bulk RNA sequencing data can be found under NCBI SRA BioProject PRJNA1060927 (SAMN39250368 to SAMN39250382), the single cell RNA sequencing data under NCBI SRA BioProject PRJNA1060254 (SAMN39223008 to SAMN39223016). The processed Seurat single cell dataset will be made available. The newly described *Platynereis* genes from this transcriptome are listed with their GenBank identifiers in Supplementary Data 2.

Code Availability

The code used for processing and visualizing the bulk- and single cell data presented in this manuscript will be made available on GitHub.

Acknowledgements

The authors are grateful to members of their respective research groups for continuous input into this project; Alison Cole (University of Vienna) and Simon Haendeler (CIBIV, University of Vienna) for advice on single-cell data processing; Kevin Nzumbi Mutemi and Detlev Arendt (EMBL, Heidelberg) for access to the *Platynereis dumerilii* genome sequence and primary annotations; Margaryta Borisova, Andrij Belokurov and Netsanet Getachew (University of Vienna) for animal supply; the Max Perutz Labs BioOptics Facility for access to advanced light microscopy and FACS; the ImagoSeine core facility of Institut Jacques Monod, a member of France BioImaging (ANR-10-INBS-04) and certified IBiSA platform and the Next Generation Sequencing services at the Vienna BioCenter Core Facilities for service and advice.

Funding

This research has been supported by a joint grant from the Agence Nationale de Recherche (ANR) ANR-16-CE91-0007 (G.B.) and the Austrian Science Funds (FWF) I2972 (F.R.; doi: 10.55776/I2972), the FWF Special Research Project F78 (F.R.; doi:10.55776/F78), the Fondation ARC pour la recherche sur le cancer (grant LSP 190375) (G.B.), the FWF doc.Funds PhD programme DOC 72 "Stem Cells, Tissues, Organoids – Dissecting Regulators of Potency and Pattern Formation (SCORPION)" (F.R.; doi:10.55776/DOC72), a post-doctoral fellowship of the Laboratory of Excellence (LABEX) "Who am I?" ANR-11-LABX-0071 (B.D.O.), the Austrian Academy of Sciences (ÖAW) DOC fellowship programme (A.W.S.), the German Academic Scholarship Foundation (L.A.), and the University of Vienna Research Platform "Single Cell Regulation of Stem Cells (SinCeReSt)" (F.R.). For open access purposes, F.R. has

applied a CC BY public copyright license to any author accepted manuscript version arising from this submission.

Competing interests

The authors declare no competing interests.

References

1. Bely, A. E. & Nyberg, K. G. Evolution of animal regeneration: re-emergence of a field. *Trends Ecol. Evol.* **25**, 161–170 (2010).

2. Lai, A. G. & Aboobaker, A. A. EvoRegen in animals: Time to uncover deep conservation or convergence of adult stem cell evolution and regenerative processes. *Dev. Biol.* **433**, 118–131 (2018).

3. Srivastava, M. Beyond Casual Resemblances: Rigorous Frameworks for Comparing Regeneration Across Species. *Annu. Rev. Cell Dev. Biol.* **37**, 1–26 (**20**21).

4. Reddien, P. W. & Alvarado, A. S. Fundamentals of planarian regeneration. Annu. Rev. Cell Dev. Biol. 20, 725–757 (2004).

5. Tanaka, E. M. & Reddien, P. W. The Cellular Basis for Animal Regeneration. *Dev. Cell* **21**, 172–185 (2011).

6. Tanaka, E. M. The Molecular and Cellular Choreography of Appendage Regeneration. Cell **165**, 1598–1608 (2016).

7. Tajer, B., Savage, A. M. & Whited, J. L. The salamander blastema within the broader context of metazoan regeneration. *Front. Cell Dev. Biol.* **11**, 1206157 (2023).

8. Özpolat, B. D. & Bely, A. E. *Developmen*tal and molecular biology of annelid regeneration: a comparative review of recent studies. *Curr. Opin. Genet. Dev.* **40**, 144–153 (2016).

9. Özpolat, B. D. *et al.* The Nereid on the rise: *Platynereis* as a model system. *EvoDevo* **12**, 10 (2021).

10. Kostyuchenko, R. P. & Kozin, V. V. Comparative Aspects of Annelid Regeneration: Towards Understanding the Mechanisms of Regeneration. *Genes* **12**, 1148 (2021).

11. Nikanorova, D. D., Kupriashova, E. E. & Kostyuchenko, R. P. Regeneration in Annelids: *Cell* Sources, Tissue Remodeling, and Differential Gene Expression. *Russ. J. Dev. Biol.* **51**, 148–161 (2020).

12. Bely, A. E., Zattara, E. E. & Sikes, J. M. Regeneration in spiralians: evolutionary patterns and developmental processes. *Int. J. Dev. Biol.* **58**, 623–634 (2015).

13. Zantke, J., Bannister, S., Rajan, V. B. V., Raible, F. & Tessmar-Raible, K. Genetic and Genomic Tools for the Marine Annelid *Platynereis dumerilii*. *Genetics* **197**, 19–31 (2014).

14. Bannister, S. et al. TALENs Mediate Efficient and Heritable Mutation of Endogenous Genes in the Marine Annelid *Platynereis dumerilii*. Genetics 197, 77–89 (2014).

15. Backfisch, B., Kozin, V. V., Kirchmaier, S., Tessmar-Raible, K. & Raible, F. Tools for Gene-Regulatory Analyses in the Marine Annelid *Platynereis dumerilii*. *PLoS ONE* **9**, e93076 (2014).

16. Ćorić, A. et al. A Fast And Versatile Method for Simultaneous HCR, Immunohistochemistry And Edu Labeling (SHInE). *Integr. Comp. Biol.* **63**, 372–381 (2023).

17. Hauenschild, C. & Fischer, A. *Platynereis dumerilii*. Mikroskopische Anatomie, Fortpflanzung, Entwicklung. *Großes Zoologisches Praktikum* **10b**, (1969).

1111 18. Gazave, E. et al. Posterior elongation in the annelid *Platynereis dumerilii* involves stem
1112 cells molecularly related to primordial germ cells. Dev. Biol. **382**, 246–267 (2013).
1113 19. Juliano, C. E., Swartz, S. Z. & Wessel, G. M. A conserved germline multipotency
1114 program. *Development* **137**, 4113–4126 (2010).
1115 20. Bely, A. E. Early Events in Annelid Regeneration: A Cellular Perspective. *Am. Zoöl.* **54**,
1116 688–699 (2014).
1117 21. Planques, A., Malem, J., Parapar, J., Vervoort, M. & Gazave, E. Morphological, cellular
1118 and molecular characterization of posterior regeneration in the marine annelid *Platynereis*
1119 *dumerilii*. Dev. Biol. **445**, 189–210 (2019).
1120 22. Lin, T.-Y. et al. Fibroblast dedifferentiation as a determinant of successful regeneration.
1121 *Dev. Cell* **56**, 1541-1551.e6 (2021).
1122 23. Hofmann, D. K. Untersuchungen zur Regeneration des Hinterendes bei *Platynereis*
1123 *dumerilii*. *Zool Jb Abt Allg Zool Physiol* 374–430 (1966).
1124 24. Planques, A. et al. DNA methylation atlas and machinery in the developing and
1125 regenerating annelid *Platynereis dumerilii*. *BMC Biol.* **19**, 148 (2021).
1126 25. Paré, L. et al. Transcriptomic landscape of posterior regeneration in the annelid
1127 *Platynereis dumerilii*. *BMC Genom.* **24**, 583 (2023).
1128 26. Hicks, S. C., Townes, F. W., Teng, M. & Irizarry, R. A. Missing data and technical
1129 variability in single-cell RNA-sequencing experiments. *Biostatistics* **19**, 562–578 (2018).
1130 27. García-Castro, H. et al. ACME dissociation: a versatile cell fixation-dissociation method
1131 for single-cell transcriptomics. *Genome Biol.* **22**, 89 (2021).
1132 28. McInnes, L., Healy, J. & Melville, J. UMAP: Uniform Manifold Approximation and
1133 Projection for Dimension Reduction. *arXiv* (2018) doi:10.48550/arxiv.1802.03426.
1134 29. McGinnis, C. S., Murrow, L. M. & Gartner, Z. J. DoubletFinder: Doublet Detection in
1135 Single-Cell RNA Sequencing Data Using Artificial Nearest Neighbors. *Cell Syst.* **8**, 329-
1136 **337**.e4 (2019).
1137 30. Brunet, T. et al. The evolutionary origin of bilaterian smooth and striated myocytes.
1138 *eLife* **5**, e19**6**07 (2016).
1139 31. Zakrzewski, A.-C. et al. Early Divergence, Broad Distribution, and High Diversity of
1140 Animal Chitin Synthases. *Genome Biol. Evol.* **6**, 316–325 (2014).
1141 32. Zakrzewski, A. Molecular characterization of chaetae formation in annelida and other
1142 Lophotrochozoa. (Freie Universität Berlin, Germany, 2011).
1143 33. Song, S. et al. Globins in the marine annelid *Platynereis dumerilii* shed new light on
1144 hemoglobin evolution in bilaterians. *BMC Evol. Biol.* **20**, 165 (2020).
1145 34. Kostyuchenko, R. P. & Kozin, V. V. Morphallaxis versus Epimorphosis? Cellular and
1146 Molecular Aspects of Regeneration and Asexual Reproduction in Annelids. *Biol. Bull.* **47**,
1147 237–246 (2020).
1148 35. Kostyuchenko, R. P., Kozin, V. V., Filippova, N. A. & Sorokina, E. V. FoxA expression
1149 pattern in two polychaete species, *Alitta virens* and *Platynereis dumerilii*: Examination of
1150 the conserved key regulator of the gut development from cleavage through larval life,

postlarval growth, and regeneration. *Dev. Dyn.* **248**, 728–743 (2019).
36. Demilly, A., Steinmetz, P., Gazave, E., Marchand, L. & Vervoort, M. Involvement of the Wnt/β-catenin pathway in neurectoderm architecture in Platynereis dumerilii. *Nat. Commun.* **4**, 19**15** (2013).
37. Vanhoutte, D. et al. Thrombospondin expression in myofibers stabilizes muscle membranes. eLife 5, e**175**89 (2016).
38. Orr, A. W., Pallero, M. A., Xiong, W.-C. & Murphy-Ullrich, J. E. Thrombospondin Induces RhoA Inactivation through FAK-dependent Signaling to Stimulate Focal Adhesion Disassembly*. *J. Biol. Chem.* **279**, 48983–48992 (2004).
39. El-Kholy, S. E., Afifi, B., El-Husseiny, I. & Seif, A. Octopamine signaling via OctαR is essential for a well-orchestrated climbing performance of adult *Drosophila melanogaster*. *Sci. Rep.* **12**, 14024 (2022).
40. Vega-Macaya, F., Manieu, C., Valdivia, M., Mlodzik, M. & Olguín, P. Establishment of the Muscle–Tendon Junction During Thorax Morpho*genesis* in *Drosophila* Requires the Rho-Kinase. Genetics **204**, **11**39–1149 (2016).
41. Pfeifer, K., Dorresteijn, A. W. C. & Fröbius, A. C. Activation of Hox genes during caudal regeneration of the polychaete annelid *Platynereis dumerilii*. *Dev. Genes Evol.* **222**, 165–179 (2012).
42. Balavoine, G. Segment formation in Annelids: patterns, processes and evolution. Int. J. Dev. Biol. 58, 469–483 (2015).
43. Gulati, G. S. et al. Single-cell transcriptional diversity is a hallmark of developmental potential. *Science* **367**, 405–411 (2020).
44. Percharde, M., Bulut-Karslioglu, A. & Ramalho-Santos, M. Hypertranscription in Development, Stem Cells, and Regeneration. Dev. Cell 40, 9–21 (2017).
45. Kim, Y.-K. et al. Absolute scaling of single-cell transcriptomes identifies pervasive hypertranscription in adult stem and progenitor cells. *Cell Rep.* **42**, 111978 (2023).
46. Choi, H. M. T. et al. Third-generation in situ hybridization chain reaction: multiplexed, quantitative, sensitive, versatile, robust. Development **145**, dev165753 (2018).
47. Grimmel, J., Dorresteijn, A. W. C. & Fröbius, A. C. Formation of body appendages during caudal regeneration in *Platynereis dumerilii*: adaptation of conserved molecular toolsets. EvoDevo 7, 10 (2016).
48. Raible, F. et al. Vertebrate-Type Intron-Rich Genes in the Marine Annelid *Platynereis dumerilii*. Science **310**, 1325–1326 (2005).
49. Saudemont, A. et al. Complementary striped expression patterns of NK homeobox genes during segment formation in the annelid *Platynereis*. Dev. Biol. **317**, 430–443 (2008).
50. Ackermann, C., Dorresteijn, A. & Fischer, A. Clonal domains in postlarval *Platynereis dumerilii* (Annelida: Polychaeta). *J. Morphol.* **266**, 258–280 (2005).
51. Fischer, A. H. L. & Arendt, D. Mesoteloblast-Like Mesodermal Stem Cells in the Polychaete Annelid *Platynereis dumerilii* (Nereididae). *J. Exp. Zoöl. Part B: Mol. Dev. Evol.*

1191 **320**, 94–104 (2013).
1192 52. Özpolat, B. D., Handberg-Thorsager, M., Vervoort, M. & Balavoine, G. Cell lineage and
1193 cell cycling analyses of the 4d micromere using live imaging in the marine annelid
1194 *Platynereis dumerilii*. eLife 6, e30463 (2017).
1195 53. Chou, H.-C., Pruitt, M. M., Bastin, B. R. & Schneider, S. Q. A transcriptional blueprint for
1196 a spiral-cleaving embryo. BMC Genom. 17, 552 (2016).
1197 54. Dorresteijn, A. W. C. Quantitative analysis of cellular differentiation during early
1198 embryogenesis of *Platynereis dumerilii*. *Roux's Arch. Dev. Biol.* **199**, 14–30 (1990).
1199 55. Elgin, S. C. R. & Reuter, G. Position-Effect Variegation, Heterochromatin Formation, and
1200 Gene Silencing in *Drosophila*. *Cold Spring Harb. Perspect. Biol.* **5**, a017780 (2013).
1201 56. Takashima, S., Aghajanian, P., Younossi-Hartenstein, A. & Hartenstein, V. Origin and
1202 dynamic lineage characteristics of the developing *Drosophila* midgut stem cells. Dev. Biol.
1203 **416**, 347–360 (2016).
1204 57. Zhulyn, O. et al. Evolutionarily divergent mTOR remodels translatome for tissue
1205 regeneration. *Nature* **620**, 163–171 (2023).
1206 58. Johnson, K., Bateman, J., DiTommaso, T., Wong, A. Y. & Whited, J. L. Systemic cell cycle
1207 activation is induced following complex tissue injury in axolotl. Dev. Biol. 4**33**, 461–472
1208 (2018).
1209 59. Hirose, K., Shiomi, T., Hozumi, S. & Kikuchi, Y. Mechanistic target of rapamycin complex
1210 1 signaling regulates cell proliferation, cell survival, and differentiation in regenerating
1211 zebrafish fins. *BMC Dev. Biol.* **14**, 42 (2014).
1212 60. Molinaro, A. M., Lindsay-Mosher, N. & Pearson, B. J. Identification of TOR-responsive
1213 slow-cycling neoblasts in planarians. *EMBO Rep.* **22**, e50292 (2021).
1214 61. Peiris, T. H. et al. TOR signaling regulates planarian stem cells and controls localized
1215 and organismal growth. *J. Cell Sci.* **125**, 1657–1665 (2012).
1216 62. Lund-Ricard, Y., Cormier, P., Morales, J. & Boutet, A. mTOR Signaling at the Crossroad
1217 between Metazoan Regeneration and Human Diseases. *Int. J. Mol. Sci.* **21**, 2718 (2020).
1218 63. Tsujimoto, K., Takamatsu, H. & Kumanogoh, A. The Ragulator complex: delving its
1219 multifunctional impact on metabolism and beyond. *Inflamm. Regen.* **43**, 28 (2023).
1220 64. Bulut-Karslioglu, A. et al. The Transcriptionally Permissive Chromatin State of
1221 Embryonic Stem Cells Is Acutely Tuned to Translational Output. *Cell Stem Cell* **22**, 369-
1222 383.e8 (2018).
1223 65. Chresta, C. M. et al. AZD8055 Is a Potent, Selective, and Orally Bioavailable ATP-
1224 Competitive Mammalian Target of Rapamycin Kinase Inhibitor with In vitro and In vivo
1225 Antitumor Activity. *Cancer Res.* **70**, 288–298 (2010).
1226 66. Shao, Y. et al. Genome and single-cell RNA-sequencing of the earthworm *Eisenia*
1227 *andrei* identifies cellular mechanisms underlying regeneration. Nat. Commun. 11, 2656
1228 (2020).
1229 67. Wagner, D. E., Wang, I. E. & Reddien, P. W. Clonogenic Neoblasts Are Pluripotent
1230 Adult Stem Cells That Underlie Planarian Regeneration. Science **332**, 811–816 (2011).

68. Reddien, P. W. The Cellular and Molecular Basis for Planarian Regeneration. Cell 175, 327–345 (2018).
69. Varley, Á., Horkan, H. R., McMahon, E. T., Krasovec, G. & Frank, U. Pluripotent, germ cell competent adult stem cells underlie cnidarian regenerative ability and clonal growth. *Curr. Biol.* **33**, 1883-1892.e3 (2023).
70. Holstein, T. W. The *Hydra* stem cell system – Revisited. *Cells Dev.* **174**, 203846 (2023).
71. Álvarez-Campos, P. et al. Annelid adult cell type diversity and their pluripotent cellular origins. Nat. Commun. 15, 3194 (2024).
72. Denes, A. S. et al. Molecular Architecture of Annelid Nerve Cord Supports Common Origin of Nervous System Centralization in Bilateria. Cell **129**, 277–288 (2007).
73. Smith, K. N., Singh, A. M. & Dalton, S. Myc Represses Primitive Endoderm Differentiation in Pluripotent Stem Cells. Cell Stem Cell 7, 343–354 (2010).
74. Bernabé-Rubio, M. et al. Myc-dependent dedifferentiation of Gata6+ epidermal cells resembles reversal of terminal differentiation. *Nat. Cell Biol.* **25**, 1426–1438 (2023).
75. Koh, F. M. et al. Emergence of hematopoietic stem and progenitor cells involves a Chd1-dependent increase in total nascent transcription. *Proc. Natl. Acad. Sci.* **112**, E1734–E1743 (2015).
76. Bideau, L. et al. Variations in cell plasticity and proliferation underlie distinct modes of regeneration along the antero-posterior axis in the annelid *Platynereis*. Development **151**, (2024).
77. Satoh, A., Cummings, G. M. C., Bryant, S. V. & Gardiner, D. M. Neurotrophic regulation of fibroblast dedifferentiation during limb skeletal regeneration in the axolotl (*Ambystoma mexicanum*). Dev. Biol. 337, 444–457 (2010).
78. Satoh, A., Gardiner, D. M., Bryant, S. V. & Endo, T. Nerve-induced ectopic limb blastemas in the axolotl are equivalent to amputation-induced blastemas. Dev. Biol. **312**, 231–244 (2007).
79. Nohno, T. et al. A Chicken Homeobox Gene Related to *Drosophila* paired Is Predominantly Expressed in the Developing Limb. Dev. Biol. **158**, 254–264 (1993).
80. Logan, M. et al. Expression of Cre recombinase in the developing mouse limb bud driven by a Prxl enhancer. genesis 33, 77–80 (2002).
81. Gerber, T. et al. Single-cell analysis uncovers convergence of cell identities during axolotl limb regeneration. Science **362**, eaaq0681 (2018).
82. Zantke, J. et al. Circadian and Circalunar Clock Interactions in a Marine Annelid. Cell Rep. 5, 99–113 (2013).
83. Martin, M. Cutadapt removes adapter sequences from high-throughput sequencing reads. *EMBnetJ.* **17**, 10–12 (2011).
84. Andrews, S. FastQC: A Quality Control Tool for High Throughput Sequence Data. http://www.bioinformatics.babraham.ac.uk/projects/fastqc/ (2010).
85. Ewels, P., Magnusson, M., Lundin, S. & Käller, M. MultiQC: summarize analysis results for multiple tools and samples in a single report. *Bioinformatics* **32**, **30**47–3048 (2016).

86. Dobin, A. et al. STAR: ultrafast universal RNA-seq aligner. Bioinformatics **29**, 15–21 (2012).
87. Liao, Y., Smyth, G. K. & Shi, W. featureCounts: an efficient general purpose program for assigning sequence reads to genomic features. Bioinformatics 30, 923–930 (2014).
88. Love, M. I., Huber, W. & Anders, S. Moderated estimation of fold change and dispersion for RNA-seq data with DESeq2. Genome Biol. 15, 550 (2014).
89. Kumar, L. & Futschik, M. E. Mfuzz: A software package for soft clustering of microarray data. *Bioinformation* **2**, 5–7 (2007).
90. Wickham, H. *Ggplot2: Elegant Graphics for Data Analysis*. (Springer-Verlag, New York, 2016).
91. Mutemi, K. N. *et al.* A genome resource for the marine annelid Platynereis dumerilii. *bioRxiv* 2024.06.21.600153 (2024)
92. Stuart, T. & Satija, R. Integrative single-cell analysis. *Nat. Rev. Genet.* **20**, 257–272 (2019).
93. Steger, J. et al. Single-cell transcriptomics identifies conserved regulators of neuroglandular lineages. Cell Rep. **40**, 111370 (2022).
94. Zhang, Z., Schwartz, S., Wagner, L. & Miller, W. A Greedy Algorithm for Aligning DNA Sequences. *J. Comput. Biol.* **7**, 203–214 (2000).
95. Letunic, I., Khedkar, S. & Bork, P. SMART: recent updates, new developments and status in 2020. *Nucleic Acids Res.* **49**, gkaa937- (2020).
96. Yamaguchi, K. D. et al. IFN-β-regulated genes show abnormal expression in therapy-naïve relapsing–remitting MS mononuclear cells: Gene expression analysis employing all reported protein–protein interactions. *J. Neuroimmunol.* **195**, 116–120 (2008).
97. Zyla, J. et al. Gene set enrichment for reproducible science: comparison of CERNO and eight other algorithms. Bioinformatics **35**, 5146–5154 (2019).
98. Nguyen, L.-T., Schmidt, H. A., Haeseler, A. von & Minh, B. Q. IQ-TREE: A Fast and Effective Stochastic Algorithm for Estimating Maximum-Likelihood Phylogenies. *Mol. Biol. Evol.* **32**, 268–274 (2015).
99. Trifinopoulos, J., Nguyen, L.-T., von Haeseler, A. & Minh, B. Q. W-IQ-TREE: a fast online phylogenetic tool for maximum likelihood analysis. Nucleic Acids Res. **44**, W232–W2**35** (2016).
100. Hoang, D. T., Chernomor, O., Haeseler, A. von, Minh, B. Q. & Vinh, L. S. UFBoot2: Improving the Ultrafast Bootstrap Approximation. Mol. Biol. Evol. 35, 518–522 (2018).
101. Letunic, I. & Bork, P. Interactive Tree Of Life (iTOL) v5: an online tool for phylogenetic tree display and annotation. Nucleic Acids Res. 49, gkab301- (2021).
102. Blanco-Carmona, E. Generating publication ready visualizations for Single Cell transcriptomics using SCpubr. *bioRxiv* 2022.02.28.482303 (2022) doi:10.**110**1/2022.02.28.482303.
103. Kuehn, E. et al. Segment number threshold determines juvenile onset of germline cluster expansion in *Platynereis dumerilii*. J. Exp. Zoöl. Part B: Mol. Dev. Evol. **338**, 225–240

(2022).
104. Tessmar-Raible, K., Steinmetz, P. R. H., Snyman, H., Hassel, M. & Arendt, D. Fluorescent two-color whole mount in situ hybridization in Platynereis dumerilii (Polychaeta, Annelida), an emerging marine molecular model for evolution and development. *Biotechniques* **39**, 460–464 (2005).
105. Schindelin, J. et al. Fiji: an open-source platform for biological-image analysis. *Nat. Methods* **9**, **6**76–682 (2012).
106. Gibson, D. G. et al. Enzymatic assembly of DNA molecules up to several hundred kilobases. Nat. Methods 6, 343–345 (2009).
107. Backfisch, B. et al. Stable transgenesis in the marine annelid *Platynereis dumerilii* sheds new light on photoreceptor evolution. Proc. Natl. Acad. Sci. 110, 193–198 (2013).